

Multilinear Kernel Regression and Imputation via Manifold Learning

Duc Thien Nguyen and Konstantinos Slavakis*

Abstract—This paper introduces a novel nonparametric framework for data imputation, coined multilinear kernel regression and imputation via the manifold assumption (MultiL-KRIM). Motivated by manifold learning, MultiL-KRIM models data features as a point cloud located in or close to a user-unknown smooth manifold embedded in a reproducing kernel Hilbert space. Unlike typical manifold-learning routes, which seek low-dimensional patterns via regularizers based on graph-Laplacian matrices, MultiL-KRIM builds instead on the intuitive concept of tangent spaces to manifolds and incorporates collaboration among point-cloud neighbors (regressors) directly into the data-modeling term of the loss function. Multiple kernel functions are allowed to offer robustness and rich approximation properties, while multiple matrix factors offer low-rank modeling, integrate dimensionality reduction, and streamline computations with no need of training data. Two important application domains showcase the functionality of MultiL-KRIM: time-varying-graph-signal (TVGS) recovery, and reconstruction of highly accelerated dynamic-magnetic-resonance-imaging (dMRI) data. Extensive numerical tests on real and synthetic data demonstrate MultiL-KRIM’s remarkable speedups over its predecessors, and outperformance over prevalent “shallow” data-imputation techniques, with a more intuitive and explainable pipeline than deep-image-prior methods.

Index Terms—Imputation, regression, nonparametric, kernel, manifold, graph, MRI

I. INTRODUCTION

Missing data occur frequently across different fields, such as recommender systems [1], remote sensing [2], sensor networks [3], and accelerated medical imaging [4], [5], inflicting bias and deficiency on downstream data-analysis tasks. Amidst a wide range of strategies for data imputation, *imputation-by-regression* is one of the most popular frameworks, where measured data act as regressors while missing data are imputed by the fitted regression model and measured data [6].

Imputation of missing data is typically viewed as a matrix/tensor completion problem, since (dynamic) images, or spatio-temporal data of sensor networks are usually arranged into matrices/tensors. Popular data-imputation approaches are compressed sensing, e.g., [7], and low-rank methods which are realized via a decomposition of the data matrix into low-rank matrix factors [8], [9]. On the other hand, dictionary learning [10]–[13] factorizes the data matrix into an over-complete (“fat”) matrix and a sparse one. Sequential multi-layer factorization of the data matrix has been also reported [14]. Non-linear activation function can be also applied to those layers, resulting into deep matrix factorizations [15], [16],

similarly to deep neural networks. Tensors can be reshaped (“flattened”) into matrices to enjoy the tools of matrix completion. However, there exist concepts of multilinear rank inherent to tensors, such as the CP and Tucker rank, yielding CP and Tucker tensor decompositions [17]. Recently, tensor networks offer generalized tensor decompositions [18]–[20]. All of the aforementioned methods fall under the umbrella of parametric modeling, where the characteristic is that model dimensions, that is, inner dimensions of the matrix/tensor factorizations, do not scale with the number of the observed data.

Another recently popular path of parametric modeling is deep learning (DeepL), e.g., [21], [22]. Nevertheless, not only is DeepL usually training-data hungry and computationally heavy, but concerns were also raised in [23] about instabilities in medical-image reconstruction. Deep image priors (DIP) [24] and untrained neural networks offer user-defined priors to alleviate the need for massive training data, and have been used in signal recovery [25], [26] and accelerated medical imaging [27], [28].

In contrast to the previous parametric methods, nonparametric regression operates without any priors and statistical assumptions on the data in an effort to reduce as much as possible the bias inflicted on data modeling by the user [29]. The price to be paid for this distribution-free approach is that the dimensions of the nonparametric-regression model scales with the number of observed data. Within nonparametric-regression methods, the kernel-based ones stand out thanks to their highly intuitive and explainable functional forms to approximate involved non-linear functions [30]–[34]. The crux is to use a non-linear feature mapping $\varphi(\cdot)$ to map data from their input space to a high-, even infinite-dimensional feature space, where linear operations are used to reflect non-linear operations in the original input space. If the feature space is chosen to be a reproducing kernel Hilbert space (RKHS) \mathcal{H} , with well-known and versatile properties in approximation theory [35], inner products in \mathcal{H} can be calculated via simple functional evaluations in the input space (“kernel trick”) [36].

Aiming at learning methods for high-dimensional data, manifold learning (ManL) offers a framework where data/features are considered to be points in or close to a low-dimensional (non-linear) smooth manifold \mathcal{M} embedded in a high-dimensional ambient space [37]. ManL affords many degrees of freedom in data modeling because it adopts a minimal number of assumptions; no specifics of \mathcal{M} are presumed other than its smoothness. ManL identifies low-dimensional data patterns to effect dimensionality reduction. More specifically, “local approaches,” including local linear embedding (LLE) [38] and Laplacian eigenmaps [39], effect dimensionality reduction

*D. T. Nguyen and K. Slavakis are with the Department of Information and Communications Engineering, Tokyo Institute of Technology, Yokohama, 226-8502 Japan (e-mails: {nguyen.t.au, slavakis.k.aa}@m.titech.ac.jp).

by preserving local proximity among data, while “global approaches,” such as ISOMAP [40], preserve geodesic distances between all pairs of points. While local approaches may fail to capture long-range dependencies in the point-cloud, global ones are usually computationally costly. The standard ManL route for data imputation is to use a graph Laplacian matrix to model the interdependencies among the rows/columns of the data matrix [41], [42]. This approach has been widely used in recommender systems [43]–[45] to construct users/items interaction. Due to the focus on “locality” by the graph Laplacian matrix, the computed interpolation functions appear to be non-continuous at sampled points, especially in cases of severe under-sampling [46].

Different from parametric modeling and motivated by ManL, this paper develops a generalization, abbreviated hereafter *MultiLinear Kernel Regression and Imputation via the Manifold assumption (MultiL-KRIM)*, of the nonparametric kernel-based approach of [47], [48]. Features are assumed to form a point-cloud which lies in or close to a smooth manifold \mathcal{M} embedded in an RKHS \mathcal{H} . Unlike popular decomposition-based methods, such as low-rank- [49], [50], tensor-based [51], [52] and dictionary learning [10]–[13], which promote a “blind decomposition” of the data matrix/tensor, and unlike standard ManL routes which are based on Laplacian-matrix-based regularization of a regression loss [41], [42], MultiL-KRIM explores collaborative-filtering and tangent-space modeling ideas to extract and at the same time incorporate latent feature geometry *directly* into data-matrix decompositions. MultiL-KRIM needs no training data to operate, belongs to the family of nonparametric regression to reduce its dependence on the probability distribution of the data as much as possible [29], and offers an explainable and simple geometric learning paradigm, unlike the majority of DeepL schemes which are based on perplexed and cascading non-linear function layers.

Unlike its bilinear predecessors BiLMDM [47] and KRIM [48], where dimensionality-reduction *pre-steps* are detached from the regression task, MultiL-KRIM affords multiple matrix factors to allow dimensionality reduction be employed directly into the regression task by letting its inverse-problem automatically identify the “optimal low-dimensional” rendition of a kernel matrix. In addition, MultiL-KRIM leverages its flexible matrix factors for higher computational efficiency in its inverse-problem algorithmic solution.

To showcase the functionality of MultiL-KRIM, two imputation tasks, corresponding to different application domains, are considered: (i) the recently popular problem of time-varying graph-signal (TVGS) recovery (Section IV), and (ii) signal reconstruction in dynamic magnetic resonance imaging (dMRI) under severe under-sampling (Section V). This manuscript extends the short paper [53], which considers the dMRI case. The extensive numerical tests in Sections IV and V illustrate that MultiL-KRIM outperforms various state-of-the-art “shallow” parametric and nonparametric methods.

The rest of the paper is organized as follows. Section II describes rigorously the missing-data imputation problem and briefly introduces state-of-the-art techniques. Section III presents the MultiL-KRIM data modeling, its inverse problem and an algorithmic solution. Finally, Section VI summarizes

the paper and provides hints about future research directions. To abide by the Journal’s page limits for a first paper submission, several of the discussions are moved into the accompanying supplementary file.

II. THE IMPUTATION-BY-REGRESSION PROBLEM AND PRIOR ART

Data are arranged in an N -mode tensor \mathcal{Y} of size $I_1 \times I_2 \times \cdots \times I_N$, where $\{I_n\}_{n=1}^N \subset \mathbb{N}_*$ (\mathbb{N}_* is the set of all positive integers). The observed data take values from the set of all complex numbers \mathbb{C} , while entries of \mathcal{Y} which correspond to missing data are set to be equal to $+\infty$. In other words, $\mathcal{Y} \in (\mathbb{C} \cup \{+\infty\})^{I_1 \times I_2 \times \cdots \times I_N}$.

Tensor \mathcal{Y} can be *unfolded/matricized/flattened* along mode k into a matrix $\mathbf{Y}_{(k)}$ [17]. For simplicity, assume that \mathcal{Y} is unfolded along mode N , and $\mathbf{Y} := \mathbf{Y}_{(N)} \in (\mathbb{C} \cup \{+\infty\})^{I_0 \times I_N}$, where $I_0 := I_1 I_2 \cdots I_{N-1}$. Let the (i, t) th entry of \mathbf{Y} be denoted by $y_{it} := [\mathbf{Y}]_{it}$. Denote also the rows and columns of \mathbf{Y} as $\mathcal{Z} := \{\mathbf{z}_i\}_{i=1}^{I_0}$ and $\mathcal{V} := \{\mathbf{v}_t\}_{t=1}^{I_N}$, respectively; that is, $\mathbf{Y} = [\mathbf{z}_1, \dots, \mathbf{z}_{I_0}]^\top = [\mathbf{v}_1, \dots, \mathbf{v}_{I_N}]$, where \top denotes vector/matrix transposition. For rigorous discussions, let the index set of observed entries $\Omega := \{(i, t) \in \{1, \dots, I_0\} \times \{1, \dots, I_N\} \mid y_{it} \neq +\infty\}$, and define the linear *sampling mapping* $\mathcal{S}_\Omega: (\mathbb{C} \cup \{+\infty\})^{I_0 \times I_N} \rightarrow \mathbb{C}^{I_0 \times I_N}: \mathbf{Y} \mapsto \mathcal{S}_\Omega(\mathbf{Y})$, which operates entry-wisely as follows: $[\mathcal{S}_\Omega(\mathbf{Y})]_{it} := [\mathbf{Y}]_{it}$, if $(i, t) \in \Omega$, while $[\mathcal{S}_\Omega(\mathbf{Y})]_{it} := 0$, if $(i, t) \notin \Omega$.

To cover a wide range of application domains, it is assumed that data \mathbf{Y} , observed in a input-data domain $\mathcal{D}_y \subset (\mathbb{C} \cup \{+\infty\})^{I_0 \times I_N}$, possess also a representation over another domain $\mathcal{D}_x \subset \mathbb{C}^{I_0 \times I_N}$, and that the “link” between \mathcal{D}_y and \mathcal{D}_x is a transform mapping $\mathcal{T}: \mathcal{D}_x \rightarrow \mathcal{D}_y$, which is usually considered to be invertible. In other words, it is assumed that there exists an $\mathbf{X} \in \mathcal{D}_x \subset \mathbb{C}^{I_0 \times I_N}$ such that (s.t.) $\mathcal{T}(\mathbf{X})$ agrees with $\mathbf{Y} \in \mathcal{D}_y$ on its observed entries at positions Ω . For example, in the context of Section V, \mathcal{D}_y is the k -space domain and \mathcal{D}_x is the image one, with \mathcal{T} being the two-dimensional discrete Fourier transform (DFT) \mathcal{F} [5]. In cases where there is no need for the extra domain \mathcal{D}_x (see Section IV), then $\mathcal{D}_x := \mathcal{D}_y$, and \mathcal{T} is set to be the identity mapping Id.

Typically, imputation-by-regression is achieved by solving the inverse problem

$$\min_{\mathbf{X} \in \mathbb{C}^{I_0 \times I_N}} \mathcal{L}(\mathbf{X}) + \mathcal{R}(\mathbf{X}) \quad (1a)$$

$$\text{s.t. } \mathcal{S}_\Omega(\mathbf{Y}) = \mathcal{S}_\Omega \mathcal{T}(\mathbf{X}) \quad (1b)$$

and other constraints,

where $\mathcal{L}(\cdot)$ is a loss that incorporates the user-defined data model into the design, and $\mathcal{R}(\cdot)$ is the regularizer used to impose structural priors to the data model. Moreover, (1b) is the “data-consistency” constraint. A popular strategy for low-rank models is to have data consistency appear as the “soft” loss $\mathcal{L}(\mathbf{X}) := \|\mathcal{S}_\Omega(\mathbf{Y}) - \mathcal{S}_\Omega \mathcal{T}(\mathbf{X})\|_F^2$ in (1a), where $\|\cdot\|_F$ stands for the Frobenius norm of a matrix, together with the nuclear-norm regularizer $\mathcal{R}(\mathbf{X}) := \|\mathbf{X}\|_*$ [7], instead of using the “hard” constraint in (1b). Although such a path can be also addressed by the proposed MultiL-KRIM, the present manuscript keeps the “hard” constraint in (1b) to allow for

$\mathcal{L}(\cdot)$ obtain simpler, “cleaner,” and more familiar expressions than those after involving the operator \mathcal{S}_Ω in $\mathcal{L}(\cdot)$.

A popular low-rank data model is expressed by the loss $\mathcal{L}(\mathbf{X}, \mathbf{U}, \mathbf{V}) = \|\mathbf{X} - \mathbf{U}\mathbf{V}\|_{\mathbb{F}}^2$, where \mathbf{U} and \mathbf{V} are added as auxiliary variables to the inverse problem (1), with \mathbf{U} having more rows than columns [8], [9]. In contrast, if \mathbf{U} is over-complete, i.e., more columns than rows, and \mathbf{V} is sparse, the previous loss yields dictionary learning [11]. More generally, the loss $\|\mathbf{X} - \mathbf{U}_1\mathbf{U}_2\cdots\mathbf{U}_Q\mathbf{V}\|_{\mathbb{F}}^2$, where all of \mathbf{X} , $\{\mathbf{U}_q\}_{q=1}^Q$ and \mathbf{V} are variables to be optimized, leads to multi-layer matrix factorization (MMF) [14], which serves as a multilinear representation of the data. With regards to multilinear algebra, inverse problems can also be formulated directly on the tensor \mathcal{Y} , where tensor-decomposition frameworks such as Tucker and CP decomposition [17], or the more recent tensor networks [18]–[20], replace the standard matrix ones. All of the aforementioned parametric factorization schemes are “blind,” in a sense that all matrix/tensor factors are variables to be computed, and no data/feature geometry is incorporated in the data model. Typically, any prior knowledge and additional model assumptions are realized via the regularizer $\mathcal{R}(\cdot)$.

The nonparametric basis pursuit (NBP) [30] introduces the following data-modeling loss

$$\mathcal{L}(\mathbf{X}, \mathbf{B}, \mathbf{C}) = \|\mathbf{X} - \mathbf{K}_{\mathcal{Z}}\mathbf{B}\mathbf{C}\mathbf{K}_{\mathcal{Y}}\|_{\mathbb{F}}^2, \quad (2)$$

where $[\mathbf{K}_{\mathcal{Z}}]_{i'i''} = \kappa_{\mathcal{Z}}(\mathbf{z}_{i'}, \mathbf{z}_{i''})$ and $[\mathbf{K}_{\mathcal{Y}}]_{t't''} = \kappa_{\mathcal{Y}}(\mathbf{y}_{t'}, \mathbf{y}_{t''})$ are kernel matrices, generated by the rows \mathcal{Z} and columns \mathcal{Y} , with reproducing kernel functions $\kappa_{\mathcal{Z}}(\cdot, \cdot)$ and $\kappa_{\mathcal{Y}}(\cdot, \cdot)$ corresponding to some user-defined RKHSs $\mathcal{H}_{\mathcal{Z}}$ and $\mathcal{H}_{\mathcal{Y}}$, respectively. A very short primer on RKHSs can be found in Appendix A (supplementary file). The motivation behind (2) is model $x_{it} \approx \sum_{k=1}^d f_k(\mathbf{z}_i)g_k(\mathbf{y}_t)$, where $f_k := \sum_{i'=1}^{I_0} b_{i'k}\varphi_{\mathcal{Z}}(\mathbf{z}_{i'}) \in \mathcal{H}_{\mathcal{Z}}$, $g_k := \sum_{t'=1}^{I_N} c_{kt'}\varphi_{\mathcal{Y}}(\mathbf{y}_{t'}) \in \mathcal{H}_{\mathcal{Y}}$, with $\varphi_{\mathcal{Z}}$ and $\varphi_{\mathcal{Y}}$ being feature maps (see Appendix A), and $d \leq \min\{I_0, I_N\}$ is a user-defined upper bound on \mathbf{X} 's rank. Matrices \mathbf{B} and \mathbf{C} in (2) gather all coefficients $\{b_{i'k}\}$ and $\{c_{kt'}\}$, respectively. Similarly to NBP [30], kernel graph learning (KGL) [54] assumes the loss $\mathcal{L}(\mathbf{X}, \mathbf{G}) = \|\mathbf{X} - \mathbf{K}_{\mathcal{Z}}\mathbf{G}\mathbf{K}_{\mathcal{Y}}\|_{\mathbb{F}}^2$, which yields (2) by decomposing \mathbf{G} as the product $\mathbf{B}\mathbf{C}$ of low-rank matrices. Moreover, kernel regression over graphs (KRG) [55] adopts the loss $\mathcal{L}(\mathbf{X}, \mathbf{H}) = \|\mathbf{X} - \mathbf{H}\mathbf{K}_{\mathcal{Y}}\|_{\mathbb{F}}^2$, which yields NBP and KGL by decomposing \mathbf{H} into $\mathbf{K}_{\mathcal{Z}}\mathbf{B}\mathbf{C}$ and $\mathbf{K}_{\mathcal{Z}}\mathbf{G}$, respectively. To avoid alternating minimization for solving for the bilinear (2), [33] proposed the loss $\mathcal{L}(\mathbf{X}, \boldsymbol{\gamma}) = \|\text{vec}(\mathbf{X}) - \mathbf{K}_{\otimes}\boldsymbol{\gamma}\|_{\mathbb{F}}^2$, where \mathbf{K}_{\otimes} is the Kronecker product $\mathbf{K}_{\mathcal{Y}} \otimes \mathbf{K}_{\mathcal{Z}}$ and $\text{vec}(\mathbf{X})$ is the vectorization of \mathbf{X} . Although [33] offers an efficient closed-form solution, its data modeling lacks low-rankness and bilinearity. Along the lines of KRG [55] and motivated by LLE [38], [56] introduces $\mathcal{L}(\mathbf{X}, \mathbf{H}, \mathbf{F}, \mathbf{Q}) = \|\mathbf{X} - \mathbf{H}\mathbf{K}_{\mathbb{F}}\|_{\mathbb{F}}^2 + \|\mathbf{F} - \mathbf{Q}\mathbf{K}_{\mathcal{Y}}\|_{\mathbb{F}}^2$, where the kernel matrix $\mathbf{K}_{\mathbb{F}}$ is defined by the low-dimensional representation \mathbf{F} of \mathbf{X} . This method requires two optimization steps per iteration, first on (\mathbf{H}, \mathbf{Q}) , and then on (\mathbf{X}, \mathbf{F}) .

Notice that kernel matrices $\mathbf{K}_{\mathcal{Z}}, \mathbf{K}_{\mathcal{Y}}$ are square, with their dimensions scaling with the dimensions of \mathbf{X} . This causes the scaling of the dimensions of the parameter matrices $\mathbf{B}, \mathbf{C}, \mathbf{G}$, and \mathbf{H} with the dimensions of the data, which is characteristic of nonparametric methods, but at the same time

raises significant computational obstacles in cases of high-dimensional data. In fact, the CPU setting, used in this study for numerical validations, was not able to carry through the NBP computations for the high-dimensional data of Section V. Moreover, all approximating functions $\{f_k\}$ and $\{g_k\}$ in NBP, KGL, and KRG are only required to belong to some RKHSs, without any consideration of more elaborate geometric and ManL arguments.

III. DATA MODELING BY MULTI-L-KRIM

As a first step (see Figure 1), MultiL-KRIM extracts geometric information from a subset of the observed data, coined “navigator data” and denoted hereafter as $\check{\mathbf{Y}}_{\text{nav}} := [\check{\mathbf{y}}_1^{\text{nav}}, \dots, \check{\mathbf{y}}_{N_{\text{nav}}}^{\text{nav}}] \in \mathbb{C}^{\nu \times N_{\text{nav}}}$, for some $\nu, N_{\text{nav}} \in \mathbb{N}_*$. Their specific definition depends on the application domain. For example, navigator data can be vectorized patches from the heavily sampled region of an image, or, in a network with time-series data, they can be samples of time-series collected from a subset of the network nodes. This approach of extracting geometric information from the data themselves, without imposing any user-defined statistical priors, and incorporating the extracted information into MultiL-KRIM's inverse problem differs from “blind” decomposition methods, e.g., [10]–[13], [49]–[52] (see also Section I), where no geometric information from the data is infused into their inverse problems.

As the number of navigator data points N_{nav} grows for large datasets, to avoid computational complexity issues, a subset $\{\mathbf{l}_k\}_{k=1}^{N_l}$, coined *landmark/representative* points, with $N_l \leq N_{\text{nav}}$, is selected from $\{\check{\mathbf{y}}_k^{\text{nav}}\}_{k=1}^{N_{\text{nav}}}$ (see Figure 1). To avoid interrupting the flow of the discussion, several strategies to form navigator data $\check{\mathbf{Y}}_{\text{nav}}$ and to select landmark points $\{\mathbf{l}_k\}_{k=1}^{N_l}$ are deferred to Section IV-C. Let $\check{\mathbf{L}} := [\mathbf{l}_1, \mathbf{l}_2, \dots, \mathbf{l}_{N_l}] \in \mathbb{C}^{\nu \times N_l}$. Motivated by ManL, this study assumes that there is some latent geometry hidden within $\{\check{\mathbf{y}}_k^{\text{nav}}\}_{k=1}^{N_{\text{nav}}}$ and consequently $\{\mathbf{l}_k\}_{k=1}^{N_l}$, which manifests itself in an appropriately user-defined feature space \mathcal{H} . Here, \mathcal{H} is taken to be an RKHS, associated with a reproducing kernel $\kappa(\cdot, \cdot) : \mathbb{C}^{\nu} \times \mathbb{C}^{\nu} \rightarrow \mathbb{R}$, and a feature mapping $\varphi : \mathbb{C}^{\nu} \rightarrow \mathcal{H}$ (see Appendix A in the supplementary file). By a slight abuse of notation, let $\Phi(\check{\mathbf{L}}) := [\varphi(\mathbf{l}_1), \dots, \varphi(\mathbf{l}_{N_l})]$, where $\varphi(\mathbf{l}_k) \in \mathcal{H}, \forall k \in \{1, \dots, N_l\}$ (see Figure 2).

The (i, t) th entry x_{it} of \mathbf{X} is modeled as

$$[\mathbf{X}]_{it} = x_{it} \approx f_i(\check{\boldsymbol{\mu}}_t) = \langle f_i \mid \varphi(\check{\boldsymbol{\mu}}_t) \rangle_{\mathcal{H}}, \quad (3)$$

where $f_i(\cdot) : \mathbb{C}^{\nu} \rightarrow \mathbb{C}$ is an unknown non-linear function in the RKHS functional space \mathcal{H} , $\check{\boldsymbol{\mu}}_t$ is an unknown vector in \mathbb{C}^{ν} , and the latter part of (3) is because of the reproducing property of \mathcal{H} [35]. It is assumed that f_i and $\varphi(\check{\boldsymbol{\mu}}_t)$ belong to the linear span of $\{\varphi(\mathbf{l}_k)\}_{k=1}^{N_l}$, i.e., there exist complex-valued $N_l \times 1$ vectors $\mathbf{d}_i := [d_{i1}, \dots, d_{iN_l}]^{\top}$ and $\mathbf{b}_t := [b_{t1}, \dots, b_{tN_l}]^{\top}$ s.t.

$$f_i = \sum_{k=1}^{N_l} d_{ik}\varphi(\mathbf{l}_k) = \Phi(\check{\mathbf{L}})\mathbf{d}_i, \quad (4a)$$

$$\varphi(\check{\boldsymbol{\mu}}_t) = \sum_{k=1}^{N_l} b_{kt}\varphi(\mathbf{l}_k) = \Phi(\check{\mathbf{L}})\mathbf{b}_t. \quad (4b)$$

Altogether, by back-substitutions into (3),

$$x_{it} \approx \langle \Phi(\check{\mathbf{L}})\mathbf{d}_i \mid \Phi(\check{\mathbf{L}})\mathbf{b}_t \rangle_{\mathcal{H}} = \mathbf{d}_i^{\text{H}}\mathbf{K}_{\mathbf{b}_t}\mathbf{b}_t, \quad (5)$$

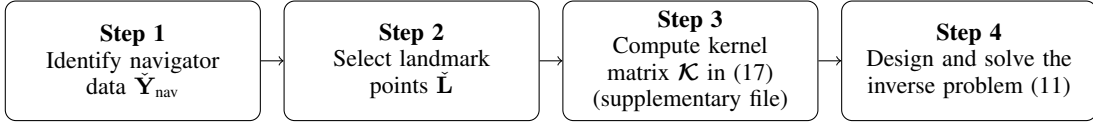


Fig. 1: Pipeline of MultiL-KRIM

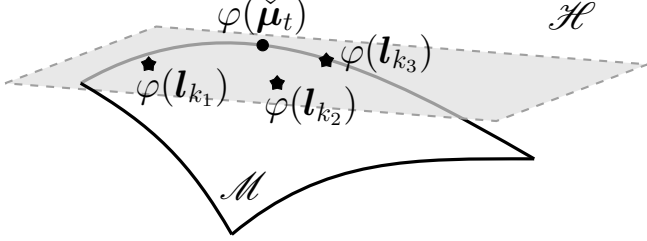


Fig. 2: The manifold-learning (ManL) modeling assumption: points $\{\varphi(\mathbf{l}_k)\}_{k=1}^{N_l}$ lie into or close to an unknown-to-the-user smooth manifold \mathcal{M} which is embedded into an ambient RKHS \mathcal{H} . The “collaborative-filtering” modeling assumption: only a few points, $\{\varphi(\mathbf{l}_{k_n})\}_{n=1}^3$ here, collaborate *affinely* to approximate $\varphi(\check{\boldsymbol{\mu}}_t)$. The small number of “collaborating neighbors” implies a low-dimensional structure. All affine combinations of $\{\varphi(\mathbf{l}_{k_n})\}_{n=1}^3$ define the approximating “linear patch” (affine hull, gray-colored plane), which mimics the concept of a tangent space to \mathcal{M} .

where \mathbf{K} is the complex-valued $N_l \times N_l$ matrix whose (k, k') -th entry is equal to $\langle \varphi(\mathbf{l}_k) | \varphi(\mathbf{l}_{k'}) \rangle_{\mathcal{H}} = \kappa(\mathbf{l}_k, \mathbf{l}_{k'})$, and superscript H stands for complex conjugate transposition. To offer a simple data model and compact notations, if $\mathbf{D} := [\mathbf{d}_1, \dots, \mathbf{d}_{I_0}]^H \in \mathbb{C}^{I_0 \times N_l}$ and $\mathbf{B} := [\mathbf{b}_1, \dots, \mathbf{b}_{I_N}] \in \mathbb{C}^{N_l \times I_N}$ are the parameters that need to be identified, then data are modeled as the bilinear form

$$\mathbf{X} \approx \mathbf{D} \mathbf{K} \mathbf{B}. \quad (6)$$

So far, (4) follow the standard subspace-modeling assumption of kernel methods, met also in the prior nonparametric designs NBP [30], KRG [55] and KGL [54] (see also the discussion after (2)): both f_i and $\varphi(\check{\boldsymbol{\mu}}_t)$ are assumed to belong to a linear subspace spanned by $\{\varphi(\mathbf{l}_k)\}_{k=1}^{N_l}$. However, inspired by ManL and [47], [48], and in quest for low-dimensional structures, MultiL-KRIM takes the standard kernel modeling assumptions a few steps further: points $\{\varphi(\mathbf{l}_k)\}_{k=1}^{N_l}$ are assumed to lie into or close to an unknown-to-the-user smooth manifold \mathcal{M} which is embedded into an ambient RKHS \mathcal{H} (see Figure 2). Furthermore, a “collaborative-filtering” modeling flavor is added to the design: only a few points within $\{\varphi(\mathbf{l}_k)\}_{k=1}^{N_l}$ ($\{\varphi(\mathbf{l}_{k_n})\}_{n=1}^3$ in Figure 2) collaborate *affinely* to approximate $\varphi(\check{\boldsymbol{\mu}}_t)$. Affine combinations, expressed via $\mathbf{1}_{N_l}^H \mathbf{b}_t = 1$, where $\mathbf{1}_{N_l}$ is the $N_l \times 1$ all-one vector, are motivated by the fundamental concept of tangent spaces (“linear patches”, simply put) to smooth manifolds [57]. Moreover, the assumption that only a small number of “collaborating neighbors” is sufficient to approximate $\varphi(\check{\boldsymbol{\mu}}_t)$, expressed explicitly by considering a sparse vector \mathbf{b}_t , is motivated by the desire to identify low-dimensional structures within $\{\varphi(\mathbf{l}_k)\}_{k=1}^{N_l}$ and by the success of sparse approximations in low-dimensional data modeling.

Choosing $\kappa(\cdot, \cdot)$ to define \mathbf{K} requires the intensive tasks of cross validation and fine tuning. A popular and straightforward way to overcome such tasks and to generalize (6),

implemented also in [48], is via multiple kernels:

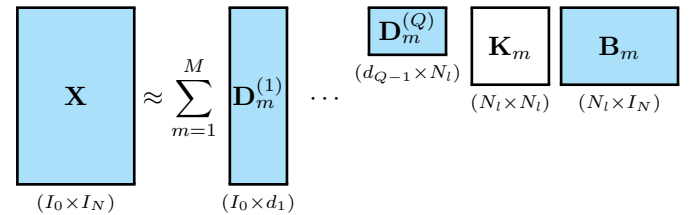
$$\mathbf{X} \approx \sum_{m=1}^M \mathbf{D}_m \mathbf{K}_m \mathbf{B}_m, \quad (7)$$

with user-defined reproducing kernels $\{\kappa_m(\cdot, \cdot)\}_{m=1}^M$, and thus kernel matrices $\{\mathbf{K}_m\}_{m=1}^M$, complex-valued $I_0 \times N_l$ matrices $\{\mathbf{D}_m\}_{m=1}^M$, and $N_l \times I_N$ matrices $\{\mathbf{B}_m\}_{m=1}^M$.

The larger the cardinality N_{nav} of the navigator data, the larger the number N_l of landmark points may become, justifying the nonparametric character of the present design. Likewise, the larger the dimensionality I_0 of the data \mathbf{Y} , the larger the number of rows of \mathbf{D}_m s in (7). In other words, for large and high-dimensional datasets (see Section V), the size $I_0 \times N_l$ of \mathbf{D}_m s may become unbearably large. To reduce computational complexity and effect low-rank structure on the approximation, KRIM [48] compressed each $N_l \times N_l$ matrix \mathbf{K}_m into a low-dimensional $d \times N_l$ ($d \ll N_l$) rendition $\check{\mathbf{K}}_m$ to yield the model $\mathbf{X} \approx \sum_{m=1}^M \check{\mathbf{D}}_m \check{\mathbf{K}}_m \mathbf{B}_m$, where $\{\check{\mathbf{D}}_m\}_{m=1}^M$ are now low-rank $I_0 \times d$ matrices. Matrix $\check{\mathbf{K}}_m$ was computed from \mathbf{K}_m via a dimensionality-reduction module (pre-step) in [48], inspired by LLE [38]. However, such a pre-step inflicts the following drawbacks on KRIM’s design: (i) with large numbers M of kernels and N_l of landmark points, the LLE-inspired pre-step raises computational obstacles, while fine-tuning its hyperparameters consumes extra effort; and (ii) if not carefully fine-tuned, the error from compressing \mathbf{K}_m into $\check{\mathbf{K}}_m$ may propagate to the next stage of KRIM’s pipeline.

The present MultiL-KRIM avoids the previous KRIM’s drawbacks by the following multilinear factorization,

$$\mathbf{X} \approx \sum_{m=1}^M \mathbf{D}_m^{(1)} \mathbf{D}_m^{(2)} \dots \mathbf{D}_m^{(Q)} \mathbf{K}_m \mathbf{B}_m, \quad (8)$$



where $\mathbf{D}_m^{(q)} \in \mathbb{C}^{d_{q-1} \times d_q}$, $d_0 := I_0$, $d_Q := N_l$, and the inner matrix dimensions $\{d_q\}_{q=1}^{Q-1}$ are user defined. Notice that for $Q = 2$, the term $\mathbf{D}_m^{(2)} \mathbf{K}_m$ may be seen as the low-dimensional $\check{\mathbf{K}}_m$ in [48]. Nonetheless, $\{\mathbf{D}_m^{(q)}\}_{(q,m)}$ are identified during a single-stage learning task, avoiding any KRIM-like pre-steps with their hyperparameter tuning and errors. It is worth stressing here that in the special case where $M = 1$, $\mathbf{K}_1 := \mathbf{I}_{N_l}$, with \mathbf{I}_{N_l} denoting the identity matrix, and with no affine and sparsity constraints on \mathbf{B}_1 , (8) yields the latent-geometry-agnostic MMF [14]. See Section IV-D for numerical tests of MultiL-KRIM vs. MMF on real-world data.

It can be verified that $Q > 1$ in (8) may offer substantial computational savings compared to the $Q = 1$ case. Indeed, the number of unknowns to be identified in (8) for $Q > 1$ is

$$N_{Q>1} = M \left(\sum_{q=1}^Q d_{q-1} d_q + I_N N_l \right), \quad (9)$$

as opposed to

$$N_{Q=1} = M(I_0 N_l + I_N N_l) \quad (10)$$

in the $Q = 1$ case. If I_0 and N_l are large, then $\{d_q\}_{q=1}^{Q-1}$ can be chosen so that $N_{Q>1} \ll N_{Q=1}$ (see Appendix Table IX (supplementary file)).

By constructing the ‘‘supermatrices’’ $\{\mathcal{D}_q\}_{q=1}^Q$, \mathcal{K} , and \mathcal{B} , which are described in Appendix B, the previous considerations yield the compact data model (16) (supplementary file). Under the previous definitions, the generic MultiL-KRIM inverse problem becomes

$$\begin{aligned} \min_{(\mathbf{X}, \{\mathcal{D}_q\}_{q=1}^Q, \mathcal{B})} & \frac{1}{2} \|\mathbf{X} - \mathcal{D}_1 \mathcal{D}_2 \cdots \mathcal{D}_Q \mathcal{K} \mathcal{B}\|_{\mathbb{F}}^2 \\ & + \underbrace{\lambda_1 \|\mathcal{B}\|_1 + \mathcal{R}_2(\mathbf{X}, \{\mathcal{D}_q\}_{q=1}^Q)}_{\mathcal{R}(\mathbf{X}, \{\mathcal{D}_q\}_{q=1}^Q, \mathcal{B})} \end{aligned} \quad (11a)$$

$$\text{s.to } \mathcal{S}_\Omega(\mathbf{Y}) = \mathcal{S}_\Omega \mathcal{T}(\mathbf{X}), \quad (11b)$$

$$\mathbf{1}_{N_l}^H \mathbf{B}_m = \mathbf{1}_{I_N}^H, \forall m \in \{1, \dots, M\}, \quad (11c)$$

$$\text{and other constraints,} \quad (11d)$$

where the ℓ_1 -norm $\mathcal{R}_1(\cdot) := \lambda_1 \|\cdot\|_1$, used here to impose sparsity on \mathcal{B} , and $\mathcal{R}_2(\cdot)$, used to enforce prior information on the model, constitute the generic regularizer $\mathcal{R} := \mathcal{R}_1 + \mathcal{R}_2$ of (1a). Constraint (11b) states the requirement for data consistency over the index set Ω of observed data values, (11c) stands for the aforementioned ManL-inspired affine combinations, and (11d) is used to conveniently include any potential application-domain specific constraint.

The pipeline of MultiL-KRIM framework is illustrated in Figure 1. To validate the proposed framework, the following sections will demonstrate two important applications, will provide solutions to specific instances of the generic inverse problem (11), and will leverage extensive numerical tests to take a thorough look at the pipeline of Figure 1.

IV. APPLICATION: TIME-VARYING GRAPH-SIGNAL RECOVERY

This section begins with an overview of the problem of time-varying graph-signal (TVGS) recovery, followed by a short review of several state-of-the-art prior works in Section IV-A. Section IV-B formulates and provides solutions to a special instance of the MultiL-KRIM’s inverse problem (11). Finally, Section IV-C compares empirically MultiL-KRIM with several state-of-the-art methods, and investigates several variations of MultiL-KRIM.

A. TVGS recovery

Graph signal processing (GSP) is an emerging field at the intersection of graph theory and signal processing [58], [59]. A graph is an abstract mathematical object equipped with

nodes/vertices and edges, where nodes correspond to entities such as sensors of a physical network or data points, and edges represent the connections/relationships between these entities. In GSP, each node is annotated with a (time-varying) signal, so that all signals gathered across all nodes constitute the so-called graph signal.

To be more specific, a graph is denoted by $G = (\mathcal{V}, \mathcal{E})$, where $\mathcal{V} := \{1, 2, \dots, I_0\}$ represents the set of I_0 nodes, and $\mathcal{E} \subseteq \mathcal{V} \times \mathcal{V}$ is the set of edges. The topology of the graph is described by the adjacency matrix $\mathbf{W} \in \mathbb{R}^{I_0 \times I_0}$, whose (i, j) th entry $w_{ij} \in \mathbb{R}_+$ denotes the edge weight between nodes i and j . In this study, G is considered to be undirected, thus, \mathbf{W} is symmetric. The graph Laplacian $I_0 \times I_0$ matrix is defined as $\mathbf{L} := \text{diag}(\mathbf{W}\mathbf{1}_{I_0}) - \mathbf{W}$, where $\mathbf{1}_{I_0}$ denotes the $I_0 \times 1$ all-one vector, and $\text{diag}(\mathbf{W}\mathbf{1}_{I_0})$ stands for the $I_0 \times I_0$ diagonal matrix whose diagonal entries are the corresponding entries of the $I_0 \times 1$ vector $\mathbf{W}\mathbf{1}_{I_0}$. The graph signal is denoted by $\mathbf{Y} = [\mathbf{y}_1, \mathbf{y}_2, \dots, \mathbf{y}_{I_N}] \in \mathbb{R}^{I_0 \times I_N}$, where the columns $\mathcal{Y} := \{\mathbf{y}_t\}_{t=1}^{I_N}$ are the graph-signal ‘‘snapshots’’ at I_N time points, while rows $\mathcal{Z} := \{\mathbf{z}_i\}_{i=1}^{I_0}$ of \mathbf{Y} are the time profiles of the I_0 signals which annotate the nodes of the graph.

The analysis of graph signals is pivotal in fields such as recommender systems [60], power grids [61], sensor [62], urban [63], and vehicular networks [64]. Due to reasons like users’ privacy, sensors fault, or resources conservation, such application domains often encounter the problem of missing data. Naturally, there have been numerous studies to address the problem, most of which leverage low-rank and smoothness assumptions on \mathbf{Y} . Typically, it is assumed that \mathbf{Y} is low rank due to dependencies among time points and/or nodes [65]. On the other hand, there are studies which adopt the graph Laplacian operator \mathbf{L} [58] to impose graph-wide (a.k.a. spatial) smoothness, i.e., neighboring nodes share similar signal attributes [66], [67]. For example, the regularization function $\mathcal{R}(\cdot)$ of both KGL and KRG (see Section II) comprises a classical Tikhonov regularizer and an \mathbf{L} -based quadratic form. Instead, NBP uses only Tikhonov regularization for $\mathcal{R}(\cdot)$. Although KGL and KRG jointly recover \mathbf{Y} and the underlying graph topology \mathbf{W} or \mathbf{L} , since this study emphasizes on TVGS recovery, \mathbf{L} is assumed to be given and fixed in the sequel. Another kernel-based regression method can be also found in [68], where kernel ridge regression is used to develop a kernel Kalman-filtering (KKF) algorithm for TVGS recovery, with an \mathbf{L} -based regularizer $\mathcal{R}(\cdot)$. Furthermore, [69], [70] introduce differential smoothness and impose low-rank structure by nuclear-norm regularizers. Low-rank-cognizant matrix factorizations have been also studied extensively [71]–[75].

By using the one-step difference operator Δ [71], study [69] introduces the spatio-temporal-smoothness regularizer $\text{tr}(\Delta^T \mathbf{X}^T \mathbf{L} \mathbf{X} \Delta)$ in the place of $\mathcal{R}(\cdot)$ in (1), where $\text{tr}(\cdot)$ stands for the trace operator. Specifically, Δ is an $I_N \times (I_N - 1)$ matrix, s.t. $[\Delta]_{i,i} = -1$, $[\Delta]_{i+1,i} = 1$ for all $i = 1, \dots, I_N - 1$, while other entries are zeros. Subsequently, [70] considered an additional low-rank constraint in the form of a nuclear-norm regularizer, which was shown to outperform other popular regularizers such as spatial $\text{tr}(\mathbf{X}^T \mathbf{L} \mathbf{X})$ and temporal $\|\mathbf{X} \Delta\|_{\mathbb{F}}^2$ smoothness [76]. On the other hand,

Algorithm 1 Solving MultiL-KRIM's inverse problem

Output: Limit point $\hat{\mathbf{X}}^{(*)}$ of sequence $(\hat{\mathbf{X}}^{(n)})_{n \in \mathbb{N}}$.

- 1: Fix $\hat{\mathbf{O}}^{(0)}$, $\gamma_0 \in (0, 1]$, and $\zeta \in (0, 1)$.
 - 2: **while** $n \geq 0$ **do**
 - 3: Available are $\hat{\mathbf{O}}^{(n)}$ ((13) for TVGS or (20) for dMRI) and γ_n .
 - 4: $\gamma_{n+1} := \gamma_n(1 - \zeta\gamma_n)$.
 - 5: Solve sub-tasks (14) for TVGS or (21) for dMRI.
 - 6: $\hat{\mathbf{O}}^{(n+1)} := \gamma_{n+1}\hat{\mathbf{O}}^{(n+1/2)} + (1 - \gamma_{n+1})\hat{\mathbf{O}}^{(n)}$.
 - 7: Set $n \leftarrow n + 1$ and go to step 2.
 - 8: **end while**
-

[77] introduces the following Sobolev-smoothness regularizer $\text{tr}(\Delta^\top \mathbf{X}^\top (\mathbf{L} + \epsilon \mathbf{I}_{I_0})^\beta \mathbf{X} \Delta)$, where $\epsilon, \beta \in \mathbb{R}_{++}$ are user-defined parameters. For convenience, denote $\mathbf{L}_\epsilon^\beta := (\mathbf{L} + \epsilon \mathbf{I}_{I_0})^\beta$. Works [69], [70], [77] use a ‘‘soft’’ data-consistency loss, i.e., the quadratic loss $(1/2)\|\mathcal{S}_\Omega(\mathbf{X}) - \mathcal{S}_\Omega(\mathbf{Y})\|_F^2$ is used instead of the ‘‘hard’’ constraint $\mathcal{S}_\Omega(\mathbf{X}) = \mathcal{S}_\Omega(\mathbf{Y})$.

The extensive numerical tests of the present study have shown that the Sobolev-smoothness regularizer is currently offering state-of-the-art performance in TVGS recovery. Consequently, to ensure fairness during numerical tests, *all* competing methods, as well as the proposed MultiL-KRIM, will be equipped hereafter with the Sobolev-smoothness regularizer.

B. The inverse problem

The inverse problem for TVGS recovery becomes a special instance of the generic (11) one. More specifically,

$$\min_{(\mathbf{X}, \{\mathcal{D}_q\}_{q=1}^Q, \mathcal{B})} \underbrace{\frac{1}{2}\|\mathbf{X} - \mathcal{D}_1 \mathcal{D}_2 \cdots \mathcal{D}_Q \mathcal{K} \mathcal{B}\|_F^2 + \lambda_1 \|\mathcal{B}\|_1}_{\mathcal{R}_1(\mathcal{B})} + \underbrace{\frac{\lambda_L}{2} \text{tr}(\Delta^\top \mathbf{X}^\top \mathbf{L}_\epsilon^\beta \mathbf{X} \Delta) + \frac{\lambda_D}{2} \sum_{q=1}^Q \|\mathcal{D}_q\|_F^2}_{\mathcal{R}_2(\mathbf{X}, \{\mathcal{D}_q\}_{q=1}^Q)} \quad (12a)$$

$$\text{s.to } \mathcal{S}_\Omega(\mathbf{Y}) = \mathcal{S}_\Omega(\mathbf{X}), \quad (12b)$$

$$\mathbf{1}_{N_i}^H \mathbf{B}_m = \mathbf{1}_{I_N}^H, \forall m \in \{1, \dots, M\}, \quad (12c)$$

where the generic regularizer in (11) becomes here $\mathcal{R}(\mathbf{X}, \{\mathcal{D}_q\}_{q=1}^Q, \mathcal{B}) := \mathcal{R}_1(\mathcal{B}) + \mathcal{R}_2(\mathbf{X}, \{\mathcal{D}_q\}_{q=1}^Q)$. In the current TVGS setting, the transform mapping \mathcal{T} in (11b) takes the form of the identity operator Id . The loss function is non-convex, and to guarantee convergence to a critical point, the successive-convex-approximation framework of [78] is utilized. The algorithm is summarized in Algorithm 1, where the following tuple of estimates $\forall n \in \mathbb{N}, \forall k \in \{0, 1\}$,

$$\hat{\mathbf{O}}^{(n+k/2)} := (\hat{\mathbf{X}}^{(n+k/2)}, \hat{\mathcal{D}}_1^{(n+k/2)}, \dots, \hat{\mathcal{D}}_Q^{(n+k/2)}, \hat{\mathcal{B}}^{(n+k/2)}), \quad (13)$$

is recursively updated via the following convex sub-tasks which need to be solved at every iteration n :

$$\hat{\mathbf{X}}^{(n+1/2)} := \arg \min_{\mathbf{X}} \frac{1}{2}\|\mathbf{X} - \hat{\mathcal{D}}_1^{(n)} \cdots \hat{\mathcal{D}}_Q^{(n)} \mathcal{K} \hat{\mathcal{B}}^{(n)}\|_F^2 + \frac{\lambda_L}{2} \text{tr}(\Delta^\top \mathbf{X}^\top \mathbf{L}_\epsilon^\beta \mathbf{X} \Delta) + \frac{\tau_X}{2}\|\mathbf{X} - \hat{\mathbf{X}}^{(n)}\|_F^2$$

$$\text{s.to } \mathcal{S}_\Omega(\mathbf{Y}) = \mathcal{S}_\Omega(\mathbf{X}), \quad (14a)$$

$$\hat{\mathcal{D}}_q^{(n+1/2)} := \arg \min_{\mathcal{D}_q} \frac{1}{2}\|\hat{\mathbf{X}}^{(n)} - \hat{\mathcal{D}}_1^{(n)} \cdots \mathcal{D}_q \cdots \hat{\mathcal{D}}_Q^{(n)} \mathcal{K} \hat{\mathcal{B}}^{(n)}\|_F^2 + \frac{\lambda_D}{2}\|\mathcal{D}_q\|_F^2 + \frac{\tau_D}{2}\|\mathcal{D}_q - \hat{\mathcal{D}}_q^{(n)}\|_F^2$$

s.to \mathcal{D}_q is block diagonal $\forall q \in \{2, \dots, Q\}$,
(14b)

$$\hat{\mathcal{B}}^{(n+1/2)} := \arg \min_{\mathcal{B}} \frac{1}{2}\|\hat{\mathbf{X}}^{(n)} - \hat{\mathcal{D}}_1^{(n)} \cdots \hat{\mathcal{D}}_Q^{(n)} \mathcal{K} \mathcal{B}\|_F^2 + \lambda_1 \|\mathcal{B}\|_1 + \frac{\tau_B}{2}\|\mathcal{B} - \hat{\mathcal{B}}^{(n)}\|_F^2$$

s.to $\mathbf{1}_{N_i}^H \mathbf{B}_m = \mathbf{1}_{I_N}^H, \forall m \in \{1, \dots, M\}$,
(14c)

where the user-defined $\tau_X, \tau_D, \tau_B \in \mathbb{R}_{++}$. Sub-task (14c) is a composite convex minimization task under affine constraints, and can be thus solved iteratively by [79], while (14a) and (14b) have closed-form solutions (see Appendix C (supplementary file)).

C. Experimental setting

MultiL-KRIM is compared against several state-of-the-art methods on TVGS recovery, such as the low-rank-and-differential-smoothness (LRDS) method [70], the Sobolev-smoothness (GraphTRSS) one [77], the nonparametric kernel-based KRG [55], KGL [54], and NBP [30], as well as the multi-layer matrix factorization (MMF) [14]. Among these, LRDS, MMF, NBP, and the proposed MultiL-KRIM promote low-rank models, while the others do not. In another view, MultiL-KRIM, NBP, MMF, KGL, and KRG are factorization/structured methods, while LRDS and GraphTRSS are unstructured. More readable categorization of methods can be found at Appendix Table V (supplementary file). Notice that numerical tests of other methods on the same datasets can be found in [55], [69], [70], [77]. MultiL-KRIM, NBP, KGL, KRG, and MMF are all solved by the successive-convex-approximation framework of [78], and realized in software by the Julia programming language [80]. The software code of LRDS and GraphTRSS can be found available online. All tests were run on an 8-core Intel(R) i7-11700 2.50GHz CPU with 32GB RAM. The following sub-sections explore all steps of the MultiL-KRIM pipeline, portrayed in Figure 1.

Performance metrics. Root mean square error (RMSE), mean absolute error (MAE), and mean absolute percentage error (MAPE) are defined in Appendix E-A (supplementary file). Detailed error values of all methods across all datasets and sampling patterns are displayed in Appendix Tables XII and XIII (supplementary file). For all error metrics RMSE, MAE, and MAPE, lower values are better. All methods are finely tuned to achieve the lowest MAE. The reported metric values are the uniform averages of 20 independent runs.

Data (Step 1 of Figure 1). Three real-world datasets are considered [69], [70], [77].

- 1) D1 (sea surface temperature): Monthly data from 1870 to 2014 are collected with a spatial resolution of 1° latitude \times 1° longitude global grid. 500-month data of 100 random locations on the Pacific ocean are selected. The dimensions of data \mathbf{Y} are $(I_0, I_N) = (100, 500)$.

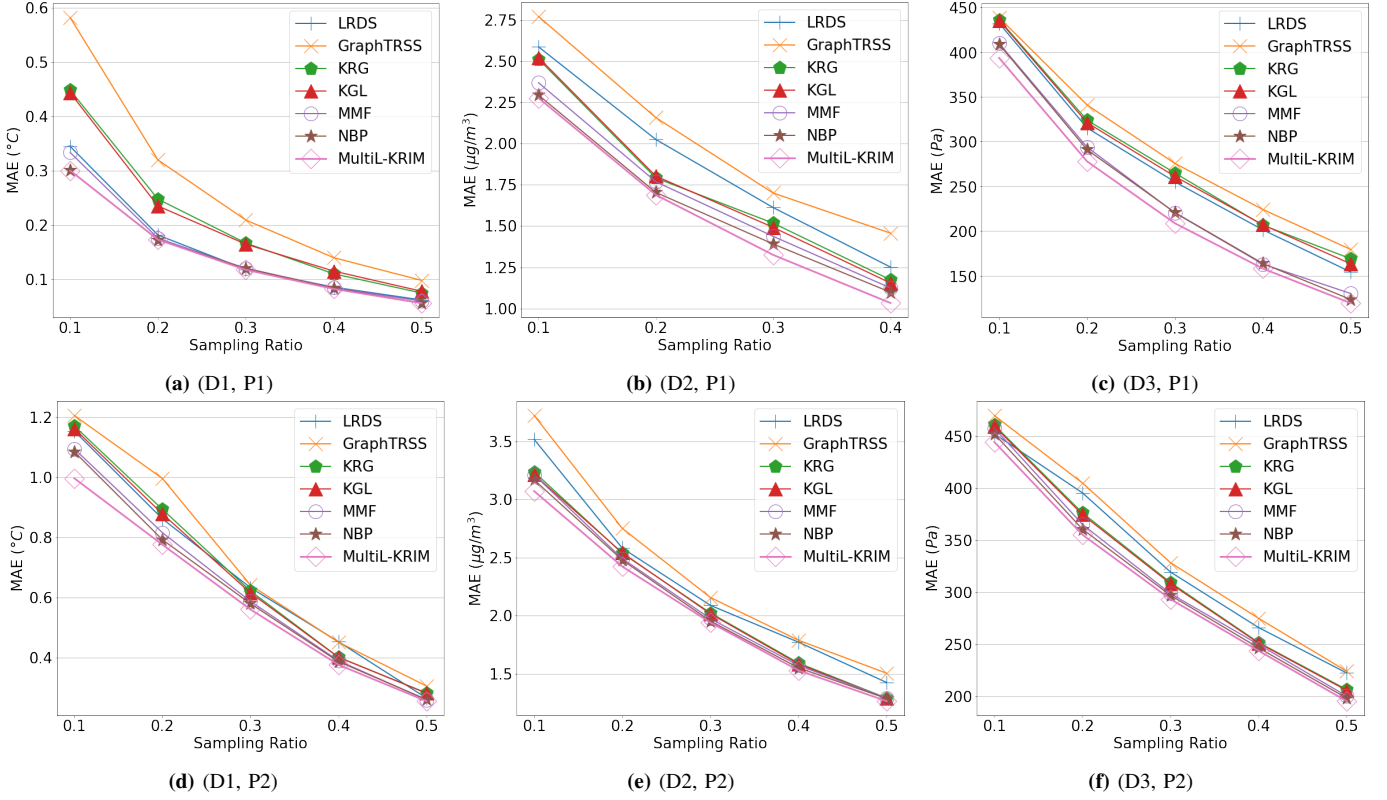


Fig. 3: Performance of MultiL-KRIM vs. other methods on different datasets (D1, D2, D3) and sampling patterns (P1, P2).

TABLE I: Average error metrics over sampling ratios in all datasets for sampling schemes P1 and P2. The best and second-best performing methods on each category are shown in red and blue, respectively.

Method	Random Sampling (P1)								
	Sea Surface Temperature			PM 2.5 Concentration			Sea Level Pressure		
	MAE	RMSE	MAPE	MAE	RMSE	MAPE	MAE	RMSE	MAPE
GraphTRSS	0.2699	0.4404	0.0250	2.0212	3.5152	0.3449	291.7323	494.7112	0.0029
KRG	0.2097	0.3301	0.0195	1.7488	3.4578	0.3042	280.1288	472.0558	0.0027
KGL	0.2075	0.3287	0.0188	1.7430	3.4657	0.3025	277.5922	461.9560	0.0025
LRDS	0.1586	0.2559	0.0162	1.8688	3.4736	0.3438	271.6200	444.6673	0.0027
MMF	0.1549	0.2417	0.0147	1.6751	3.2526	0.2809	243.4078	413.8005	0.0024
NBP	0.1469	0.2242	0.0145	1.6222	3.1857	0.2726	241.5242	412.2467	0.0024
MultiL-KRIM	0.1460	0.2315	0.0148	1.5812	3.0745	0.2743	231.4998	395.8148	0.0023
Method	Entire Snapshots Sampling (P2)								
	Sea Surface Temperature			PM 2.5 Concentration			Sea Level Pressure		
	MAE	RMSE	MAPE	MAE	RMSE	MAPE	MAE	RMSE	MAPE
GraphTRSS	0.7204	1.1669	0.0751	2.3844	4.4152	0.4072	340.3902	550.2937	0.0034
KRG	0.6744	1.0759	0.0695	2.1357	4.0605	0.3862	320.8218	563.9427	0.0032
KGL	0.6682	1.0727	0.0691	2.1284	4.0418	0.3631	319.7752	553.7329	0.0032
LRDS	0.6739	1.0754	0.0702	2.2765	4.1946	0.3724	331.0909	540.7169	0.0034
MMF	0.6299	0.9938	0.0682	2.1077	4.0294	0.3668	314.2487	540.5447	0.0032
NBP	0.6214	0.9875	0.0665	2.0875	3.9952	0.3756	310.8744	528.2204	0.0031
MultiL-KRIM	0.5934	0.9566	0.0651	2.0456	3.8761	0.3738	306.3696	528.7843	0.0031

- 2) D2 (particulate matter 2.5): The California daily mean PM2.5 concentration data are collected from 93 observation sites over 200 days starting from January 1, 2015. The dimensions of data \mathbf{Y} are $(I_0, I_N) = (93, 200)$.
- 3) D3 (sea level pressure): Global sea-level pressure data were gathered between 1948 and 2010, with a spatial resolution of 2.5° latitude \times 2.5° longitude, and temporal resolution of five days. Here, data of 500 random sites over a span of 400 time units are considered. The dimensions of data \mathbf{Y} are $(I_0, I_N) = (500, 400)$.

The graph topology is constructed by the k -nearest neighbors method as in [70]. In particular, the Euclidean distance d_{ij} between any pair of sensors $i, j \in \mathcal{V}$ is calculated based on their given geographical locations. Each node $i \in \mathcal{V}$ is connected to k nearest neighbors $\mathcal{N}_i := \{i_1, i_2, \dots, i_k\} \subset \mathcal{V}$ in terms of the Euclidean distance. Thus, $(i, i_j) \in \mathcal{E}, \forall i_j \in \mathcal{N}_i$. Note that $i \notin \mathcal{N}_i$. Then, the (i, j) th entry of the adjacency matrix \mathbf{W} is given as $w_{ij} = 1/d_{ij}^2$ if $(i, j) \in \mathcal{E}$, and $w_{ij} = 0$ otherwise. Eventually, the graph Laplacian matrix \mathbf{L} is calculated as described in Section IV-A.

Sampling patterns (Step 1 of Figure 1). With sampling ratio $r \in \{0.1, 0.2, 0.3, 0.4, 0.5\}$, the following sampling patterns are considered.

- 1) P1 (random sampling) [69]: signals of $\lceil I_0 \cdot r \rceil$ randomly sampled nodes at each time instant t are observed, where $\lceil \cdot \rceil$ denotes the ceiling function.
- 2) P2 (entire-snapshots sampling) [77]: all node signals are sampled at $\lceil I_N \cdot r \rceil$ randomly chosen time instants. In other words, $\lceil I_N \cdot r \rceil$ snapshots are randomly sampled.

Navigator data formation (Step 2 of Figure 1). The navigator data $\tilde{\mathbf{Y}}_{\text{nav}}$ of size $\nu \times N_{\text{nav}}$, for some $\nu, N_{\text{nav}} \in \mathbb{N}_*$, are defined by the sampled-and-zero-padded data $\mathcal{S}_\Omega(\mathbf{Y})$ via the following configurations.

- 1) Nav1 (snapshots): $\tilde{\mathbf{Y}}_{\text{nav}}$ are defined by the snapshots of $\mathcal{S}_\Omega(\mathbf{Y})$, represented by the columns of $\mathcal{S}_\Omega(\mathbf{Y})$. For pattern P1, $\tilde{\mathbf{Y}}_{\text{nav}} := \mathcal{S}_\Omega(\mathbf{Y})$, with $\nu = I_0$ and $N_{\text{nav}} = I_N$; for pattern P2, missing snapshots are discarded, i.e., $\nu = I_0$ and $N_{\text{nav}} = I_N \cdot r$.
- 2) Nav2 (time profiles of nodes): $\tilde{\mathbf{Y}}_{\text{nav}}$ are defined by the node time profiles of $\mathcal{S}_\Omega(\mathbf{Y})$, represented by the rows of $\mathcal{S}_\Omega(\mathbf{Y})$, i.e., $\tilde{\mathbf{Y}}_{\text{nav}} := \mathcal{S}_\Omega(\mathbf{Y})^\top$, with $\nu = I_N$ and $N_{\text{nav}} = I_0$.
- 3) Nav3 (patches): for the user-defined $\delta t \in \mathbb{N}$, $\delta t < I_N/2$, and for each $i \in \mathcal{V}$, $t \in \mathbb{N}_*$, $\delta t + 1 \leq t \leq I_n - \delta t$, a ‘‘patch’’ $\mathbf{P}_{it} = \mathcal{S}_\Omega(\mathbf{Y})|_{\mathcal{N}_i \times \mathcal{N}_t}$ of size $k \times (2\delta t + 1)$ is constructed as the submatrix of $\mathcal{S}_\Omega(\mathbf{Y})$ corresponding to the rows and columns indicated by the index sets \mathcal{N}_i and \mathcal{N}_t , respectively, where \mathcal{N}_i is the k -nearest neighbors of node i retrieved upon building \mathbf{W} , and $\mathcal{N}_t := \{\tau \in \mathbb{N}_* \mid t - \delta t \leq \tau \leq t + \delta t\}$. Then, each column of the navigator data matrix $\tilde{\mathbf{Y}}_{\text{nav}}$ is a vectorized \mathbf{P}_{it} . The size of $\tilde{\mathbf{Y}}_{\text{nav}}$ is $k(2\delta t + 1) \times I_0(I_N - 2\delta t)$. As post-processing, columns with all zeros of $\tilde{\mathbf{Y}}_{\text{nav}}$ are removed. This formation offers the densest navigator point-cloud, but raises computational complexity for landmark-point selection step.
- 4) Nav4 (windows): by the same notations used in the description of Nav3, a ‘‘window’’ centered at time instant t is the submatrix $\mathcal{S}_\Omega(\mathbf{Y})|_{\mathcal{V} \times \mathcal{N}_t}$. Each column of the navigator data matrix is one vectorized window, so the size of $\tilde{\mathbf{Y}}_{\text{nav}}$ is $\nu = I_0 \cdot (2\delta t + 1)$ and $N_{\text{nav}} = I_N - 2\delta t$. Finally, drops all-zeros columns of $\tilde{\mathbf{Y}}_{\text{nav}}$.

Landmark point selection (Step 3 of Figure 1). Based on Euclidean distance between navigator data points, the following landmark-point selection strategies are examined:

- 1) L1: greedy max-min-distance (maxmin) [81],
- 2) L2: k -means clustering, and
- 3) L3: fuzzy c -means clustering, whose centroids are chosen to be the landmark points [82].

Kernel matrix construction (Step 4 of Figure 1). In the single-kernel case ($M = 1$), the kernel from Appendix Table IV (supplementary file) which yields optimal performance is used. The intercept c of the polynomial kernel (Appendix A) is set to be the entry-wise mean of the landmark points. After extensive experiments, multiple kernels ($M > 1$) did not score considerable improvement over the previous single-kernel strategy.

The next sub-sections dive into different scenarios, each of which contains four components, closely related to the steps of the pipeline. A scenario is denoted by a tuple $(\cdot, \cdot, \cdot, \cdot)$, corresponding to data, sampling pattern, navigator data formation, and landmark-point selection strategy. If an entry of the tuple is left empty, then all possible values of the component are validated. For example, (D1, P1, Nav1, \cdot) considers sea surface temperature, random sampling, snapshots, and validates all strategies L1, L2, and L3.

D. Numerical tests

1) *The sea-surface-temperature dataset:* To examine the effect of different navigator data formations and landmark-point selection strategies, tests are conducted on the (D1, P1, \cdot, \cdot) scenario, which are detailed in Appendix E-B. It is observed that Nav1 has the lowest average errors among all navigator data formations. On the other hand, there is no significant performance difference between landmark-point selection strategies L1, L2, and L3. Henceforth, consider scenario $(\cdot, \text{P1}, \text{Nav1}, \text{L1})$; consider scenarios $(\cdot, \text{P2}, \text{Nav1}, \text{L1})$ if $\lceil I_N \cdot r \rceil \geq 100$, and $(\cdot, \text{P2}, \text{Nav3}, \text{L1})$ if $\lceil I_N \cdot r \rceil < 100$.

Table I, Figures 3a and 3d show that low-rank methods outperform others under both sampling patterns. Averaged over sampling ratios, MultiL-KRIM has lower MAE values than other methods by 1% to 46% for pattern P1 and 5% to 18% for pattern P2. Among low-rank methods, the kernel-based NBP and MultiL-KRIM have slight advantages over LRDS and MMF, especially at the lowest sampling ratio of 10% (Figures 3a and 3d). The better performance of KGL and KRG over GraphTRSS highlights the usefulness of highly structured data modeling. For pattern P2, the gaps between all methods become narrow; this can also be seen from Figure 3d. Moreover, at higher sampling ratios of 40% and 50%, the performance of factorization methods converges.

2) *The PM2.5-concentration dataset:* Figures 3b and 3e show that unstructured methods LRDS and GraphTRSS score the highest errors across all sampling rates in both patterns. Unlike in the previous dataset, all structured methods outweighs LRDS under all sampling patterns and ratios. Furthermore, the merits of structured methods are emphasized at the lowest sampling ratio of 10%, where they outperform LRDS and GraphTRSS by noticeable margins. Also taken from Figures 3b and 3e, MultiL-KRIM, NBP, and MMF consistently outperform KGL and KRG in both patterns, suggesting the necessity of low-rank factorization. Compared to pattern P1, variance between all methods is smaller in P2, especially among factorization methods, which can also be observed from Table I. In addition, the average MAE value of MultiL-KRIM is lower by 3% to 22% in pattern P1, but the range of improvement is 3% to 12% in pattern P2.

3) *The sea-level-pressure dataset:* Appendix Figure 6 (supplementary file) depicts the sensitivity of MAE values to variations of the inner dimension $d_1 \in \{10, 20, 30, 40, 50, 60, 70\}$ and the choice of kernel from the dictionary in Appendix Table IV (supplementary file), under scenario (D3, P1, Nav1, L1) at sampling ratio of 10%. The lowest MAE is reached at $d_1 = 10$ and for the Gaussian kernel, almost regardless of its

parameter σ . Notice that the linear kernel gives the highest MAE across all different d_1 .

Table I, along with Figures 3c and 3f, exhibits the continued dominance of low-rank factorization methods MultiL-KRIM, NBP, and MMF. In terms of average MAE values, MultiL-KRIM outperforms the all competing methods by 4% to 21% for pattern P1, and by 1% to 10% for pattern P2. In the case of sampling pattern P1, Figure 3c illustrates a distinct gap between the low-rank factorization methods MultiL-KRIM, NBP, and MMF, compared to others. This suggests the need for both low-rank and structured modeling. From Table I, the average MAE of LRDS in the P1 case is 3% and 4% lower than that of KGL and KRG, respectively. This indicates a slight advantage of low-rank modeling over kernel modeling in pattern P1. On the flip side, Figure 3f shows the outperformance of structured methods MultiL-KRIM, NBP, MMF, KGL, and KRG, over the unstructured ones LRDS and GraphTRSS under pattern P2, advocating the interpolation strength of structured modeling.

Computationally, MultiL-KRIM is more efficient than LRDS, since LRDS requires SVD computations for nuclear-norm minimization, which are expected to inflict computational burdens if the dimensions of the dataset are large. Indeed, for dataset D3 of dimensions 500-by-400, LRDS takes on average 1384 seconds for pattern P1 and 1456 seconds for pattern P2, around three times the run time of MultiL-KRIM (444s for P1 and 492s for P2). Details on computational times can be found in Appendix Table VIII (supplementary file).

V. APPLICATION: DYNAMIC MAGNETIC RESONANCE IMAGING

This section focuses on dMRI, serving as a more detailed exposition of [53]. Section V-A defines the problem of highly-accelerated dMRI recovery, while MultiL-KRIM's inverse problem is stated in Section V-B. The numerical tests in Section V-C demonstrate that MultiL-KRIM offers significant speed-ups from its predecessor KRIM [48], with no performance losses, while outperforming state-of-the-art “shallow” learning methods.

A. DMRI-data recovery

DMRI is a common non-invasive imaging technique for tracking the motion of body organs, offering valuable insights in the fields of cardiac and neurological diagnosis [5]. All typical data-analytic bottlenecks show up in dMRI: high dimensionality of the image data, many missing data entries due to severe under-sampling to achieve high acceleration in data collection, and strong latent spatio-temporal correlations within the data because of body-organ structured movements; e.g., a beating heart [4], [5].

Naturally, there is a rich literature of imputation methods to address the highly under-sampled dMRI problem: compressed sensing [83], [84], low-rank modeling [85]–[87], and learning methods based on dictionaries [88]–[90], manifolds [42], [48], [91]–[94], kernels [48], [94]–[97], tensors [98], [99], DeepL [100], and DIP [27], [101]. Several of those methods are selected for comparisons against MultiL-KRIM in Section V-C, including the manifold-learning-based STORM [42],

the low-rank factorization with sparsity PS-Sparse [86], tensor factorization with total variation LRTC-TV [99], and the DIP-based model TDDIP [27]. STORM follows a typical ManL route and utilizes as a regularizer a quadratic loss involving the graph Laplacian matrix. PS-Sparse uses a “semi-blind” factorization of two orthogonal low-rank matrices, where one of those matrix factors is built from navigator data. LRTC-TV instead enforces a “blind” decomposition of the data matrix, and imposes low-rankness by nuclear-norm minimization. Meanwhile, TDDIP considers randomly generated points on a user-defined manifold (a helix) as the navigator data.

The “(k,t)-space/domain” dMRI data are represented by a 3-way tensor $\mathcal{Y} \in \mathbb{C}^{I_1 \times I_2 \times I_3}$ (Figure 4a), where I_1 and I_2 are the number of phase and frequency encodings of the k-space, respectively, while I_3 stands for the number of time frames. Following the general data formation of Section II, \mathbf{Y} is obtained by vectorizing each “slice/frame” \mathcal{Y}_t of \mathcal{Y} (t denotes discrete time with $t \in \{1, \dots, I_3\}$), or, $\mathbf{Y} := [\mathbf{y}_1, \dots, \mathbf{y}_{I_3}] \in \mathbb{C}^{I_0 \times I_3}$, where $I_0 := I_1 I_2$ and $\mathbf{y}_t := \text{vec}(\mathcal{Y}_t)$. Usually, the (k,t)-space data are severely under-sampled to promote highly accelerated data collection [4], and to this end, popular sampling strategies are 1-D Cartesian (Figure 4c) and radial (Figure 4d) sampling, which define the index set Ω and the sampling operator \mathcal{S}_Ω (Section II). The goal is to recover high fidelity images in the image domain, despite the large number of missing entries in the (k,t)-space. Since the end product of the dMRI recovery is an image, the linear transform mapping \mathcal{F} , introduced in Section II to map data from the image to the (k,t)-domain, becomes the 2D DFT \mathcal{F} .

B. The inverse problem

With \mathbf{X} denoting the image-domain data, the generic MultiL-KRIM's inverse problem (11) takes here the following special form:

$$\begin{aligned} \min_{(\mathbf{X}, \mathbf{Z}, \{\mathcal{D}_q\}_{q=1}^Q, \mathcal{B})} & \frac{1}{2} \|\mathbf{X} - \mathcal{D}_1 \mathcal{D}_2 \cdots \mathcal{D}_Q \mathcal{K} \mathcal{B}\|_{\text{F}}^2 + \underbrace{\lambda_1 \|\mathcal{B}\|_1}_{\mathcal{R}_1(\mathcal{B})} \\ & + \underbrace{\frac{\lambda_2}{2} \|\mathbf{Z} - \mathcal{F}_1(\mathbf{X})\|_{\text{F}}^2 + \lambda_3 \|\mathbf{Z}\|_1}_{\mathcal{R}_{21}(\mathbf{X}, \mathbf{Z})} \\ & + \underbrace{\frac{\lambda_4}{2} \sum_{q=1}^Q \|\mathcal{D}_q\|_{\text{F}}^2}_{\mathcal{R}_{22}(\{\mathcal{D}_q\}_{q=1}^Q)} \end{aligned} \quad (15a)$$

$$\text{s.t. } \mathcal{S}_\Omega(\mathbf{Y}) = \mathcal{S}_\Omega \mathcal{F}(\mathbf{X}), \quad (15b)$$

$$\mathbf{1}_{N_t}^H \mathbf{B}_m = \mathbf{1}_{I_N}^H, \forall m \in \{1, \dots, M\}, \quad (15c)$$

where the generic regularizer in (11) becomes

$$\begin{aligned} \mathcal{R}(\mathbf{X}, \mathbf{Z}, \{\mathcal{D}_q\}_{q=1}^Q, \mathcal{B}) & := \mathcal{R}_1(\mathcal{B}) + \mathcal{R}_{21}(\mathbf{X}, \mathbf{Z}) \\ & + \mathcal{R}_{22}(\{\mathcal{D}_q\}_{q=1}^Q). \end{aligned}$$

Regularizer $\mathcal{R}_{21}(\cdot, \cdot)$ is introduced to capitalize on the prior knowledge that the dataset at hand, to be used in Section V-C, records the periodic movement of a beating heart over a static background. The mapping $\mathcal{F}_1(\mathbf{X})$ stands for the temporal 1D DFT, which operates on rows of \mathbf{X} . Each row of \mathbf{X} , of length I_3 , is the time profile of a single pixel in the image domain. The periodic or static nature of each row

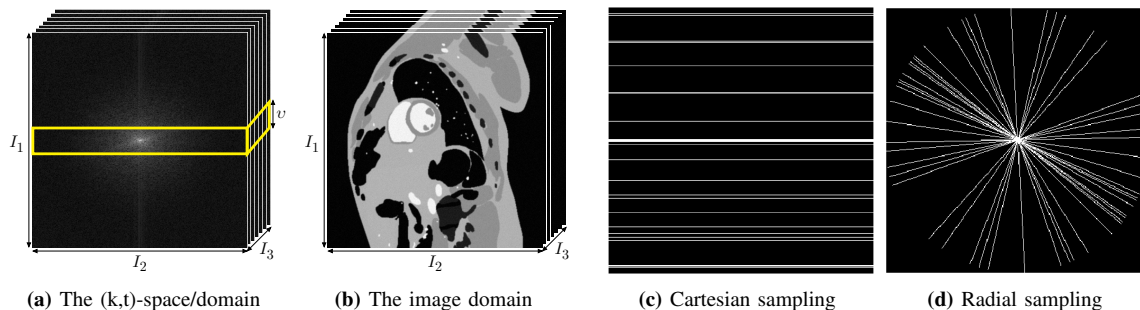


Fig. 4: (a) Domain of size $I_1 \times I_2 \times I_3$ where the dMRI data are observed and collected, with I_3 denoting the number of time frames. The marked $v \times I_2 \times I_3$ box shows the typical location of the faithful “navigator/pilot” data, corresponding, usually, to the “low-frequency” area of the domain. The “white dots” indicate the locations where data are collected, with the black-colored majority of the (k,t)-space to correspond to locations where there are missing data. After “flattening” the 3D (k,t)-space into a 2D one (see Section II), these “white dots” define the index set Ω , and thus the sampling operator \mathcal{S}_Ω . (b) The $(I_1 \times I_2 \times I_3)$ -sized image domain. The image-domain data are obtained by applying the two dimensional (2D) inverse DFT \mathcal{F}^{-1} to the (k,t)-space data [5]. (c) 1D Cartesian and (d) radial sampling trajectories in k-space. The white-colored lines indicate locations where data are collected.

of \mathbf{X} suggests that its 1D DFT is a sparse vector over the frequency domain. This observation justifies the penalty term $\|\mathbf{Z}\|_1$, well known for promoting sparsity, with \mathbf{Z} being an auxiliary matrix-valued variable used to simplify computations when solving the inverse problem. The solutions of the convex sub-tasks of the inverse problem follow a similar routine to that of Section IV-B, and are thus deferred to Appendix D (supplementary file) due to space limitations.

C. Numerical tests

Following [47], [48], [86], [93], [94], the proposed framework is validated on the magnetic resonance extended cardiac-torso (MRXCAT) cine phantom dataset [102], of size $(I_1, I_2, I_3) = (408, 408, 360)$, under both radial and Cartesian sampling. Similarly to [47], [48], the navigator data are formed by vectorizing the heavily sampled region of the (k,t)-space. In other words, the $v \times I_2$ box of each frame in Figure 4a, with $v = 4$, generates a number I_3 of $(vI_2) \times 1$ navigator vectors. Then, the maxmin strategy [81] is adopted to select $N_l := 70$ landmark points. Parameter $Q \in \{2, 3\}$, and for each Q the inner matrix dimensions of $\{\mathcal{D}_q\}_{q=1}^Q$ are set as follows: (i) if $Q = 2$, then $d_1 = 8$; and (ii) if $Q = 3$, then $(d_1, d_2) = (2, 8)$. Appendix Table IX (supplementary file) shows the number of parameter unknowns (9) for different settings of Q to emphasize the efficiency of MultiL-KRIM’s factorization. The inner-dimension parameter of the predecessor KRIM [48] is $d := 8$. Parameter $M \in \{1, 7\}$ for both MultiL-KRIM and KRIM, with choices of kernels as in [48] (see also Appendix Table IV (supplementary file)).

Besides the predecessors KRIM [48] and BiLMDM [47], MultiL-KRIM[M, Q] competes also against the low-rank tensor factorization with total variation (LRTC-TV) [99], the DIP-based TDDIP [27] (designed especially for radial sampling), the popular PS-Sparse [86] and ManL-based SToRM [42]. Tags KRIM[S] and KRIM[M] refer to [48] for the case of a single ($M = 1$) and multiple ($M > 1$) kernels, respectively. Performance of several other state-of-the-art methods and their comparison against KRIM and BiLMDM on the same dataset can be found in [47], [48]. Additionally, [47], [48] include also the validation of KRIM and BiLMDM on several other dMRI datasets. The software code for (MultiL-)KRIM and BiLMDM

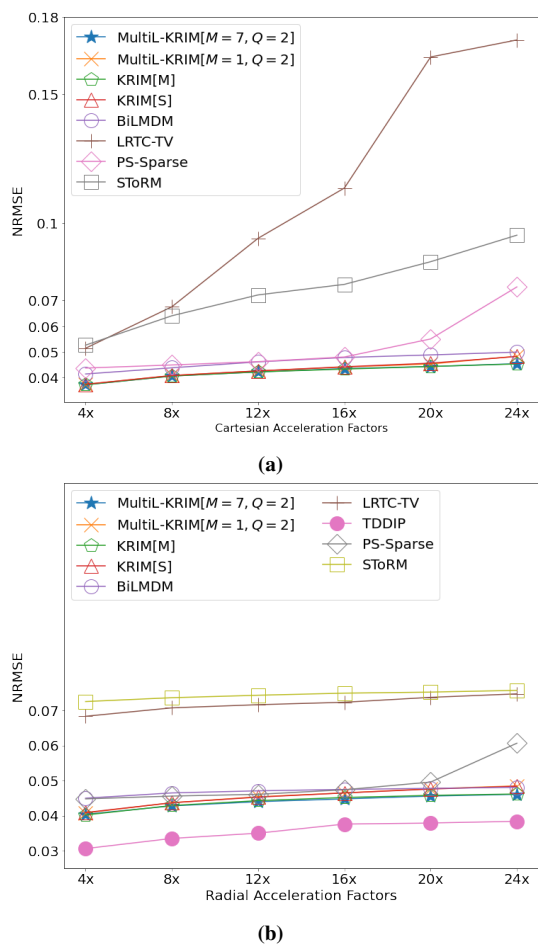


Fig. 5: Normalized RMSE values (the lower the better) w.r.t. the ground truth vs. (sampling-time) acceleration factors. An acceleration factor “ βx ” means that only $1/\beta$ of the full-scan $I_1 \times I_2$ k-space is sampled (see Figures 4c and 4d).

was written in Julia [80], while the software codes of the other methods were found available online. All tests were run on an 8-core Intel(R) i7-11700 2.50GHz CPU with 32GB RAM. As mentioned after (2), this CPU was not able to carry through NBP computations [30], since the size $I_0 \times I_0 (> 10^{10})$ entries of \mathbf{K}_Z seemed to be too large for the CPU at hand.

Performance metrics. The main evaluation metric is the normalized root mean square error $\text{NRMSE} := \|\mathbf{X} - \hat{\mathbf{X}}\|_F / \|\mathbf{X}\|_F$,

where \mathbf{X} denotes the image data obtained from fully sampled (k,t) -space data, and $\hat{\mathbf{X}}$ represents the estimate of \mathbf{X} . Additionally, reconstruction quality of high-frequency regions are quantified by the high-frequency error norm (HFEN) [88], and two sharpness measures M1 (intensity-variance based) and M2 (energy of the image gradient) [103, (43) and (46)]. Lastly, the structural similarity measure (SSIM) [104] captures local similarities between the reconstructed and the ground-truth images. Desirable outcomes are low values in NRMSE and HFEN, and high values in SSIM, M1, and M2. All methods were finely tuned to achieve the lowest NRMSE. All reported metric values are mean values of 10 independent runs.

It can be seen in Figure 5, and more precisely in Tables II and III, that MultiL-KRIM matches the performance of KRIM. Nevertheless, MultiL-KRIM shows remarkable reduction in computational time by up to 65% for multiple kernels (red-colored) and 30% for a single kernel (blue-colored). To showcase that the time reduction is because of the novel factorization approach, the reported times of KRIM[M] and KRIM[S] *do not* include the time of KRIM’s dimensionality-reduction pre-step. Furthermore, looking within MultiL-KRIM[M, Q], experiments verify that compared to when $Q = 2$, there is notable speed-up when $Q = 3$ and the inner dimensions $\{d_q\}_{q=1}^{Q-1}$ are chosen appropriately. Due to intensive fine-tuning, there is only slight difference between the single-kernel case ($M = 1$) versus the multiple-kernel case ($M = 7$). The tests also demonstrate the better performance of MultiL-KRIM over LRTC-TV, which deteriorates quickly with high acceleration rates under Cartesian sampling, and has high computational footprint due to nuclear-norm minimization. PS-Sparse is a contender with a trade-off between NRMSE and runtime, but it declines noticeably at high acceleration rates, while MultiL-KRIM does not. Additionally, structural quality measures such as SSIM and HFEN accentuate the difference between MultiL-KRIM and PS-Sparse. Although MultiL-KRIM does not reach the NRMSE and SSIM of TDDIP, it produces lower HFEN and higher sharpness measure M1, i.e., sharper images. More importantly, MultiL-KRIM offers a less computationally expensive and more data-driven approach than TDDIP, which requires a carefully handcrafted prior (manifold structure, here a helix) that does not explicitly utilize the observed data. Extra experiments on TDDIP, described in Appendix F (supplementary file), show that when the complexity of TDDIP decreases, its NRMSE and SSIM approach those of MultiL-KRIM. Albeit, increasing the number of unknowns of MultiL-KRIM, either with more kernels M or larger inner dimensions $\{d_q\}_{q=1}^{Q-1}$, does not improve its performance. These observations intrigue with a “deep” architecture for MultiL-KRIM, such as adding non-linear activation function layers into the factorization. This idea is based on the results that deep matrix factorization outperforms the standard MMF in matrix completion tasks [15], [16].

VI. CONCLUSIONS

This paper introduced MultiL-KRIM, a nonparametric (kernel-based) data-imputation-by-regression framework. Two important application domains were considered for valida-

TABLE II: Performance on Cartesian sampling (acceleration rate: 20x)

Methods \ Metrics	NRMSE	SSIM	HFEN	M1	M2	Time
MultiL-KRIM[$M = 7, Q = 2$]	0.0443	0.8698	0.1147	37.26	1.4×10^6	1.2hrs
MultiL-KRIM[$M = 1, Q = 2$]	0.0453	0.8686	0.1269	37.24	1.3×10^6	52min
MultiL-KRIM[$M = 7, Q = 3$]	0.0444	0.8695	0.1149	37.26	1.4×10^6	1.1hrs
MultiL-KRIM[$M = 1, Q = 3$]	0.0454	0.8684	0.1270	37.24	1.3×10^6	48min
KRIM[M] [48]	0.0443	0.8696	0.1136	37.34	1.4×10^6	3.3hrs
KRIM[S] [48]	0.0450	0.8670	0.1149	37.25	1.3×10^6	55min
BLMDM [47]	0.0488	0.8589	0.1423	37.08	1.3×10^6	40min
LRTC-TV [99]	0.1645	0.6943	0.4330	31.52	1.5×10^6	8.3hrs
SToRM [42]	0.0850	0.8110	0.2504	37.02	1.2×10^6	58min
PS-Sparse [86]	0.0550	0.8198	0.1483	37.18	1.2×10^6	15min

TABLE III: Performance on radial sampling (acceleration rate: 16x)

Methods \ Metrics	NRMSE	SSIM	HFEN	M1	M2	Time
MultiL-KRIM[$M = 7, Q = 2$]	0.0448	0.8680	0.1023	37.35	1.4×10^6	1.2hrs
MultiL-KRIM[$M = 1, Q = 2$]	0.0465	0.8618	0.1305	37.26	1.4×10^6	44min
MultiL-KRIM[$M = 7, Q = 3$]	0.0448	0.8675	0.1030	37.35	1.4×10^6	1hr
MultiL-KRIM[$M = 1, Q = 3$]	0.0465	0.8618	0.1305	37.26	1.4×10^6	41min
KRIM[M] [48]	0.0450	0.8670	0.1136	37.34	1.4×10^6	3hrs
KRIM[S] [48]	0.0465	0.8618	0.1301	37.26	1.4×10^6	58min
BLMDM [47]	0.0475	0.8560	0.1491	37.30	1.4×10^6	1.4hrs
TDDIP [27]	0.0376	0.8896	0.1452	36.24	1.3×10^6	3.9hrs
LRTC-TV [99]	0.0738	0.8063	0.3725	37.06	1.7×10^6	8.6hrs
SToRM [42]	0.0753	0.8319	0.3694	37.38	1.6×10^6	30min
PS-Sparse [86]	0.0496	0.7908	0.1733	37.31	1.4×10^6	15min

tion: time-varying-graph-signal (TVGS) recovery, and reconstruction of highly accelerated dynamic-magnetic-resonance-imaging (dMRI) data. Numerical tests on TVGS recovery demonstrated MultiL-KRIM’s outperformance over state-of-the-art “shallow” methods. Furthermore, via tests on dMRI data, MultiL-KRIM was shown to match the performance of its predecessor KRIM [48] with significant reduction in computational time. MultiL-KRIM outperformed state-of-the-art “shallow” methods also on dMRI data, and although it did not reach the accuracy of the deep-image-prior-based TDDIP [27], it offered a more explainable and computationally tractable path. Prospectively, to further enhance MultiL-KRIM’s performance, current research effort includes also its “deep” variations.

REFERENCES

- [1] A. Ramlatchan, M. Yang, Q. Liu, M. Li, J. Wang, and Y. Li, “A survey of matrix completion methods for recommendation systems,” *Big Data Mining and Analytics*, vol. 1, no. 4, pp. 308–323, 2018.
- [2] H. Shen, X. Li, Q. Cheng, C. Zeng, G. Yang, H. Li, and L. Zhang, “Missing information reconstruction of remote sensing data: A technical review,” *IEEE Geoscience and Remote Sensing Magazine*, vol. 3, no. 3, pp. 61–85, 2015.
- [3] J. Du, M. Hu, and W. Zhang, “Missing data problem in the monitoring system: A review,” *IEEE Sensors Journal*, vol. 20, no. 23, pp. 13984–13998, 2020.
- [4] Z.-P. Liang and P. C. Lauterbur, “An efficient method for dynamic magnetic resonance imaging,” *IEEE Trans. Medical Imaging*, vol. 13, no. 4, pp. 677–686, 1994.
- [5] Z.-P. Liang and P. C. Lauterbur, *Principles of Magnetic Resonance Imaging: A Signal Processing Perspective*. IEEE Press, 2000.
- [6] M. S. Osman, A. M. Abu-Mahfouz, and P. R. Page, “A survey on data imputation techniques: Water distribution system as a use case,” *IEEE Access*, vol. 6, pp. 63279–63291, 2018.
- [7] E. J. Candes and B. Recht, “Exact low-rank matrix completion via convex optimization,” in *2008 46th Annual Allerton Conference on Communication, Control, and Computing*, pp. 806–812, IEEE, 2008.
- [8] P. Chen and D. Suter, “Recovering the missing components in a large noisy low-rank matrix: Application to SFM,” *IEEE transactions on pattern analysis and machine intelligence*, vol. 26, no. 8, pp. 1051–1063, 2004.
- [9] Y. Koren, R. Bell, and C. Volinsky, “Matrix factorization techniques for recommender systems,” *Computer*, vol. 42, no. 8, pp. 30–37, 2009.
- [10] J. Mairal, J. Ponce, G. Sapiro, A. Zisserman, and F. Bach, “Supervised dictionary learning,” *Advances in neural information processing systems*, vol. 21, 2008.

- [11] I. Tošić and P. Frossard, "Dictionary learning," *IEEE Signal Processing Magazine*, vol. 28, no. 2, pp. 27–38, 2011.
- [12] J. Sun, Q. Qu, and J. Wright, "Complete dictionary recovery over the sphere I: Overview and the geometric picture," *IEEE Transactions on Information Theory*, vol. 63, no. 2, pp. 853–884, 2016.
- [13] J. Sun, Q. Qu, and J. Wright, "Complete dictionary recovery over the sphere II: Recovery by riemannian trust-region method," *IEEE Transactions on Information Theory*, vol. 63, no. 2, pp. 885–914, 2016.
- [14] A. Cichocki and R. Zdunek, "Multilayer nonnegative matrix factorization using projected gradient approaches," *International Journal of Neural Systems*, vol. 17, no. 06, pp. 431–446, 2007.
- [15] J. Fan and J. Cheng, "Matrix completion by deep matrix factorization," *Neural Networks*, vol. 98, pp. 34–41, 2018.
- [16] P. De Handschutter, N. Gillis, and X. Siebert, "A survey on deep matrix factorizations," *Computer Science Review*, vol. 42, p. 100423, 2021.
- [17] T. G. Kolda and B. W. Bader, "Tensor decompositions and applications," *SIAM Review*, vol. 51, no. 3, pp. 455–500, 2009.
- [18] I. V. Oseledets, "Tensor-train decomposition," *SIAM Journal on Scientific Computing*, vol. 33, no. 5, pp. 2295–2317, 2011.
- [19] Q. Zhao, G. Zhou, S. Xie, L. Zhang, and A. Cichocki, "Tensor ring decomposition," *arXiv preprint arXiv:1606.05535*, 2016.
- [20] Y.-B. Zheng, T.-Z. Huang, X.-L. Zhao, Q. Zhao, and T.-X. Jiang, "Fully-connected tensor network decomposition and its application to higher-order tensor completion," in *Proceedings of the AAAI conference on artificial intelligence*, vol. 35, pp. 11071–11078, 2021.
- [21] L. T. Nguyen, J. Kim, and B. Shim, "Low-rank matrix completion: A contemporary survey," *IEEE Access*, vol. 7, pp. 94215–94237, 2019.
- [22] J. Su, B. Xu, and H. Yin, "A survey of deep learning approaches to image restoration," *Neurocomputing*, vol. 487, pp. 46–65, 2022.
- [23] V. Antun, F. Renna, C. Poon, B. Adcock, and A. C. Hansen, "On instabilities of deep learning in image reconstruction and the potential costs of AI," *Proceedings of the National Academy of Sciences*, vol. 117, no. 48, pp. 30088–30095, 2020.
- [24] D. Ulyanov, A. Vedaldi, and V. Lempitsky, "Deep image prior," in *Proceedings of the IEEE conference on computer vision and pattern recognition*, pp. 9446–9454, 2018.
- [25] R. Heckel and M. Soltanolkotabi, "Compressive sensing with untrained neural networks: Gradient descent finds a smooth approximation," in *International Conference on Machine Learning*, pp. 4149–4158, PMLR, 2020.
- [26] S. Rey, S. Segarra, R. Heckel, and A. G. Marques, "Untrained graph neural networks for denoising," *IEEE Transactions on Signal Processing*, vol. 70, pp. 5708–5723, 2022.
- [27] J. Yoo, K. H. Jin, H. Gupta, J. Yerly, M. Stuber, and M. Unser, "Time-dependent deep image prior for dynamic MRI," *IEEE Trans. Medical Imaging*, vol. 40, no. 12, pp. 3337–3348, 2021.
- [28] Q. Zou, A. H. Ahmed, P. Nagpal, S. Kruger, and M. Jacob, "Dynamic imaging using a deep generative STORM (Gen-STORM) model," *IEEE Trans. Medical Imaging*, vol. 40, no. 11, pp. 3102–3112, 2021.
- [29] L. Györfi, M. Kohler, A. Krzyżak, and H. Walk, *A Distribution-Free Theory of Nonparametric Regression*. New York: Springer, 2010.
- [30] J. A. Bazerque and G. B. Giannakis, "Nonparametric basis pursuit via sparse kernel-based learning: A unifying view with advances in blind methods," *IEEE Signal Processing Magazine*, vol. 30, no. 4, pp. 112–125, 2013.
- [31] J. Fan and T. W. Chow, "Non-linear matrix completion," *Pattern Recognition*, vol. 77, pp. 378–394, 2018.
- [32] M. Stock, T. Pahikkala, A. Airola, B. De Baets, and W. Waegeman, "A comparative study of pairwise learning methods based on kernel ridge regression," *Neural computation*, vol. 30, no. 8, pp. 2245–2283, 2018.
- [33] P. Giménez-Febre, A. Pagès-Zamora, and G. B. Giannakis, "Matrix completion and extrapolation via kernel regression," *IEEE Transactions on Signal Processing*, vol. 67, no. 19, pp. 5004–5017, 2019.
- [34] Z. Chen, W. Zhao, and S. Wang, "Kernel meets recommender systems: A multi-kernel interpolation for matrix completion," *Expert Systems with Applications*, vol. 168, p. 114436, 2021.
- [35] N. Aronszajn, "Theory of reproducing kernels," *Trans. American Mathematical Society*, vol. 68, no. 3, pp. 337–404, 1950.
- [36] B. Schölkopf and A. J. Smola, *Learning with Kernels*. MIT press, 2002.
- [37] T. Lin and H. Zha, "Riemannian manifold learning," *IEEE Trans. Pattern Analysis and Machine Intelligence*, vol. 30, no. 5, pp. 796–809, 2008.
- [38] S. T. Roweis and L. K. Saul, "Nonlinear dimensionality reduction by locally linear embedding," *Science*, vol. 290, no. 5500, pp. 2323–2326, 2000.
- [39] M. Belkin and P. Niyogi, "Laplacian eigenmaps and spectral techniques for embedding and clustering," *NIPS*, vol. 14, 2001.
- [40] J. B. Tenenbaum, V. d. Silva, and J. C. Langford, "A global geometric framework for nonlinear dimensionality reduction," *Science*, vol. 290, no. 5500, pp. 2319–2323, 2000.
- [41] V. Kalofolias, X. Bresson, M. Bronstein, and P. Vandergheynst, "Matrix completion on graphs," *arXiv preprint arXiv:1408.1717*, 2014.
- [42] S. Poddar and M. Jacob, "Dynamic MRI using smoothness regularization on manifolds (SToRM)," *IEEE Trans. Medical Imaging*, vol. 35, no. 4, pp. 1106–1115, 2016.
- [43] H. Ma, D. Zhou, C. Liu, M. R. Lyu, and I. King, "Recommender systems with social regularization," in *Proceedings of the fourth ACM international conference on Web search and data mining*, pp. 287–296, 2011.
- [44] N. Rao, H.-F. Yu, P. K. Ravikumar, and I. S. Dhillon, "Collaborative filtering with graph information: Consistency and scalable methods," *Advances in neural information processing systems*, vol. 28, 2015.
- [45] A. Mongia and A. Majumdar, "Matrix completion on multiple graphs: Application in collaborative filtering," *Signal Processing*, vol. 165, pp. 144–148, 2019.
- [46] Z. Shi, S. Osher, and W. Zhu, "Weighted nonlocal Laplacian on interpolation from sparse data," *Journal of Scientific Computing*, vol. 73, pp. 1164–1177, 2017.
- [47] G. N. Shetty, K. Slavakis, A. Bose, U. Nakarmi, G. Scutari, and L. Ying, "Bi-linear modeling of data manifolds for dynamic-MRI recovery," *IEEE Trans. Medical Imaging*, vol. 39, no. 3, pp. 688–702, 2020.
- [48] K. Slavakis, G. N. Shetty, L. Cannelli, G. Scutari, U. Nakarmi, and L. Ying, "Kernel regression imputation in manifolds via bi-linear modeling: The dynamic-MRI case," *IEEE Trans. Computational Imaging*, vol. 8, pp. 133–147, 2022.
- [49] M. A. Davenport and J. Romberg, "An overview of low-rank matrix recovery from incomplete observations," *IEEE Journal of Selected Topics in Signal Processing*, vol. 10, no. 4, pp. 608–622, 2016.
- [50] Y. Chi, Y. M. Lu, and Y. Chen, "Nonconvex optimization meets low-rank matrix factorization: An overview," *IEEE Transactions on Signal Processing*, vol. 67, no. 20, pp. 5239–5269, 2019.
- [51] P. Zhou, C. Lu, Z. Lin, and C. Zhang, "Tensor factorization for low-rank tensor completion," *IEEE Transactions on Image Processing*, vol. 27, no. 3, pp. 1152–1163, 2017.
- [52] C. Cai, G. Li, H. V. Poor, and Y. Chen, "Nonconvex low-rank tensor completion from noisy data," *Advances in neural information processing systems*, vol. 32, 2019.
- [53] D. T. Nguyen and K. Slavakis, "Multi-linear kernel regression and imputation via manifold learning: The dynamic MRI case," in *Proc. IEEE International Conference on Acoustics, Speech and Signal Processing (ICASSP)*, (Seoul: Korea), April 14–19 2024. to be presented.
- [54] X. Pu, S. L. Chau, X. Dong, and D. Sejdinovic, "Kernel-based graph learning from smooth signals: A functional viewpoint," *IEEE Transactions on Signal and Information Processing over Networks*, vol. 7, pp. 192–207, 2021.
- [55] A. Venkitaraman, S. Chatterjee, and P. Händel, "Predicting graph signals using kernel regression where the input signal is agnostic to a graph," *IEEE Transactions on Signal and Information Processing over Networks*, vol. 5, no. 4, pp. 698–710, 2019.
- [56] M. A. Carreira-Perpin, Z. Lu, *et al.*, "Manifold learning and missing data recovery through unsupervised regression," in *Proc. IEEE International Conference on Data Mining*, pp. 1014–1019, IEEE, 2011.
- [57] J. W. Robbin and D. A. Salamon, *Introduction to Differential Geometry*. Berlin: Springer, 2022.
- [58] A. Ortega, P. Frossard, J. Kovačević, J. M. Moura, and P. Vandergheynst, "Graph signal processing: Overview, challenges, and applications," *Proceedings of the IEEE*, vol. 106, no. 5, pp. 808–828, 2018.
- [59] W. Hu, J. Pang, X. Liu, D. Tian, C.-W. Lin, and A. Vetro, "Graph signal processing for geometric data and beyond: Theory and applications," *IEEE Transactions on Multimedia*, vol. 24, pp. 3961–3977, 2021.
- [60] W. Huang, A. G. Marques, and A. R. Ribeiro, "Rating prediction via graph signal processing," *IEEE Transactions on Signal Processing*, vol. 66, no. 19, pp. 5066–5081, 2018.
- [61] R. Ramakrishna and A. Scaglione, "Grid-graph signal processing (grid-GSP): A graph signal processing framework for the power grid," *IEEE Transactions on Signal Processing*, vol. 69, pp. 2725–2739, 2021.
- [62] I. Jabłoński, "Graph signal processing in applications to sensor networks, smart grids, and smart cities," *IEEE Sensors Journal*, vol. 17, no. 23, pp. 7659–7666, 2017.

- [63] P.-A. Laharotte, R. Billot, E. Come, L. Oukhellou, A. Nantes, and N.-E. El Faouzi, "Spatiotemporal analysis of bluetooth data: Application to a large urban network," *IEEE Transactions on Intelligent Transportation Systems*, vol. 16, no. 3, pp. 1439–1448, 2014.
- [64] B. Placzek, "Selective data collection in vehicular networks for traffic control applications," *Transportation Research Part C: Emerging Technologies*, vol. 23, pp. 14–28, 2012.
- [65] J. Cheng, Q. Ye, H. Jiang, D. Wang, and C. Wang, "STCDG: An efficient data gathering algorithm based on matrix completion for wireless sensor networks," *IEEE Transactions on Wireless Communications*, vol. 12, no. 2, pp. 850–861, 2012.
- [66] S. Chen, A. Sandryhaila, J. M. Moura, and J. Kovačević, "Signal recovery on graphs: Variation minimization," *IEEE Transactions on Signal Processing*, vol. 63, no. 17, pp. 4609–4624, 2015.
- [67] S. Chen, R. Varma, A. Singh, and J. Kovačević, "Signal recovery on graphs: Fundamental limits of sampling strategies," *IEEE Transactions on Signal and Information Processing over Networks*, vol. 2, no. 4, pp. 539–554, 2016.
- [68] D. Romero, V. N. Ioannidis, and G. B. Giannakis, "Kernel-based reconstruction of space-time functions on dynamic graphs," *IEEE Journal of Selected Topics in Signal Processing*, vol. 11, no. 6, pp. 856–869, 2017.
- [69] K. Qiu, X. Mao, X. Shen, X. Wang, T. Li, and Y. Gu, "Time-varying graph signal reconstruction," *IEEE Journal of Selected Topics in Signal Processing*, vol. 11, no. 6, pp. 870–883, 2017.
- [70] X. Mao, K. Qiu, T. Li, and Y. Gu, "Spatio-temporal signal recovery based on low rank and differential smoothness," *IEEE Transactions on Signal Processing*, vol. 66, no. 23, pp. 6281–6296, 2018.
- [71] M. Roughan, Y. Zhang, W. Willinger, and L. Qiu, "Spatio-temporal compressive sensing and internet traffic matrices (extended version)," *IEEE/ACM Transactions on Networking*, vol. 20, no. 3, pp. 662–676, 2011.
- [72] L. Kong, M. Xia, X.-Y. Liu, M.-Y. Wu, and X. Liu, "Data loss and reconstruction in sensor networks," in *2013 Proceedings IEEE INFOCOM*, pp. 1654–1662, IEEE, 2013.
- [73] K. Xie, X. Ning, X. Wang, D. Xie, J. Cao, G. Xie, and J. Wen, "Recover corrupted data in sensor networks: A matrix completion solution," *IEEE Transactions on Mobile Computing*, vol. 16, no. 5, pp. 1434–1448, 2016.
- [74] X. Song, Y. Guo, N. Li, and S. Yang, "A novel approach based on matrix factorization for recovering missing time series sensor data," *IEEE Sensors Journal*, vol. 20, no. 22, pp. 13491–13500, 2020.
- [75] M. Lei, A. Labbe, Y. Wu, and L. Sun, "Bayesian kernelized matrix factorization for spatiotemporal traffic data imputation and kriging," *IEEE Transactions on Intelligent Transportation Systems*, vol. 23, no. 10, pp. 18962–18974, 2022.
- [76] X. Piao, Y. Hu, Y. Sun, B. Yin, and J. Gao, "Correlated spatio-temporal data collection in wireless sensor networks based on low rank matrix approximation and optimized node sampling," *Sensors*, vol. 14, no. 12, pp. 23137–23158, 2014.
- [77] J. H. Giraldo, A. Mahmood, B. Garcia-Garcia, D. Thanou, and T. Bouwmans, "Reconstruction of time-varying graph signals via Sobolev smoothness," *IEEE Transactions on Signal and Information Processing over Networks*, vol. 8, pp. 201–214, 2022.
- [78] F. Facchinei, G. Scutari, and S. Sagratella, "Parallel selective algorithms for nonconvex big data optimization," *IEEE Trans. Signal Processing*, vol. 63, no. 7, pp. 1874–1889, 2015.
- [79] K. Slavakis and I. Yamada, "Fejér-monotone hybrid steepest descent method for affinely constrained and composite convex minimization tasks," *Optimization*, vol. 67, no. 11, pp. 1963–2001, 2018.
- [80] J. Bezanson, A. Edelman, S. Karpinski, and V. B. Shah, "Julia: A fresh approach to numerical computing," *SIAM Review*, vol. 59, no. 1, pp. 65–98, 2017.
- [81] V. De Silva and J. B. Tenenbaum, "Sparse multidimensional scaling using landmark points," tech. rep., Stanford University, 2004.
- [82] M. Rashmi and P. Sankaran, "Optimal landmark point selection using clustering for manifold modeling and data classification," *Journal of Classification*, vol. 36, no. 1, pp. 94–112, 2019.
- [83] M. Lustig, D. Donoho, and J. M. Pauly, "Sparse MRI: The application of compressed sensing for rapid MR imaging," *Magnetic Resonance in Medicine*, vol. 58, no. 6, pp. 1182–1195, 2007.
- [84] L. Feng, L. Axel, H. Chandarana, K. T. Block, D. K. Sodickson, and R. Otazo, "XD-GRASP: Golden-angle radial MRI with reconstruction of extra motion-state dimensions using compressed sensing," *Magnetic Resonance in Medicine*, vol. 75, no. 2, pp. 775–788, 2016.
- [85] S. G. Lingala, Y. Hu, E. V. R. DiBella, and M. Jacob, "Accelerated dynamic MRI exploiting sparsity and low-rank structure: k-t SLR," *IEEE Trans. Medical Imaging*, vol. 30, no. 5, pp. 1042–1054, 2011.
- [86] B. Zhao, J. P. Haldar, A. G. Christodoulou, and Z.-P. Liang, "Image reconstruction from highly undersampled (k,t)-space data with joint partial separability and sparsity constraints," *IEEE Trans. Medical Imaging*, vol. 31, no. 9, pp. 1809–1820, 2012.
- [87] R. Otazo, E. Candes, and D. K. Sodickson, "Low-rank plus sparse matrix decomposition for accelerated dynamic MRI with separation of background and dynamic components," *Magnetic Resonance in Medicine*, vol. 73, no. 3, pp. 1125–1136, 2015.
- [88] S. Ravishanker and Y. Bresler, "MR image reconstruction from highly undersampled k-space data by dictionary learning," *IEEE Trans. Medical Imaging*, vol. 30, no. 5, pp. 1028–1041, 2010.
- [89] Y. Wang and L. Ying, "Compressed sensing dynamic cardiac cine MRI using learned spatiotemporal dictionary," *IEEE Trans. Biomedical Eng.*, vol. 61, no. 4, pp. 1109–1120, 2014.
- [90] J. Caballero, A. N. Price, D. Rueckert, and J. V. Hajnal, "Dictionary learning and time sparsity for dynamic MR data reconstruction," *IEEE Trans. Medical Imaging*, vol. 33, no. 4, pp. 979–994, 2014.
- [91] M. Usman, D. Atkinson, C. Kolbitsch, T. Schaeffter, and C. Prieto, "Manifold learning based ECG-free free-breathing cardiac CINE MRI," *J. Magnetic Resonance Imag.*, vol. 41, no. 6, pp. 1521–1527, 2015.
- [92] X. Chen, M. Usman, C. F. Baumgartner, D. R. Balfour, P. K. Marsden, A. J. Reader, C. Prieto, and A. P. King, "High-resolution self-gated dynamic abdominal MRI using manifold alignment," *IEEE Trans. Medical Imaging*, vol. 36, no. 4, pp. 960–971, 2017.
- [93] U. Nakarmi, K. Slavakis, J. Lyu, and L. Ying, "M-MRI: A manifold-based framework to highly accelerated dynamic magnetic resonance imaging," in *Proceedings of ISBI*, pp. 19–22, 2017.
- [94] U. Nakarmi, K. Slavakis, and L. Ying, "MLS: Joint manifold-learning and sparsity-aware framework for highly accelerated dynamic magnetic resonance imaging," in *Proceedings of ISBI*, pp. 1213–1216, 2018.
- [95] U. Nakarmi, Y. Wang, J. Lyu, D. Liang, and L. Ying, "A kernel-based low-rank (KLR) model for low-dimensional manifold recovery in highly accelerated dynamic MRI," *IEEE Trans. Medical Imaging*, vol. 36, no. 11, pp. 2297–2307, 2017.
- [96] S. Poddar, Y. Q. Mohsin, D. Ansah, B. Thattaliyath, R. Ashwath, and M. Jacob, "Manifold recovery using kernel low-rank regularization: application to dynamic imaging," *IEEE Trans. Computational Imaging*, vol. 5, no. 3, pp. 478–491, 2019.
- [97] O. Arif, H. Afzal, H. Abbas, M. F. Amjad, J. Wan, and R. Nawaz, "Accelerated dynamic MRI using kernel-based low rank constraint," *J. Medical Systems*, vol. 43, no. 8, p. 271, 2019.
- [98] J. Liu, P. Musialski, P. Wonka, and J. Ye, "Tensor completion for estimating missing values in visual data," *IEEE Trans. Pattern Analysis and Machine Intelligence*, vol. 35, no. 1, pp. 208–220, 2012.
- [99] X. Li, Y. Ye, and X. Xu, "Low-rank tensor completion with total variation for visual data inpainting," *Proceedings of AAAI Conference on Artificial Intelligence*, vol. 31, Feb. 2017.
- [100] F. Knoll, K. Hammernik, C. Zhang, S. Moeller, T. Pock, D. K. Sodickson, and M. Akcakaya, "Deep-learning methods for parallel magnetic resonance imaging reconstruction: A survey of the current approaches, trends, and issues," *IEEE signal processing magazine*, vol. 37, no. 1, pp. 128–140, 2020.
- [101] A. Qayyum, I. Ilahi, F. Shamsaid, F. Boussaid, M. Bennamoun, and J. Qadir, "Untrained neural network priors for inverse imaging problems: A survey," *IEEE Transactions on Pattern Analysis and Machine Intelligence*, 2022.
- [102] L. Wissmann, C. Santelli, W. P. Segars, and S. Kozierke, "MRXCAT: Realistic numerical phantoms for cardiovascular magnetic resonance," *J. Cardiovascular Magnetic Resonance*, vol. 16, no. 1, pp. 1–11, 2014.
- [103] M. Subbarao, T.-S. Choi, and A. Nikzad, "Focusing techniques," *Optical Engineering*, vol. 32, no. 11, pp. 2824–2836, 1993.
- [104] Z. Wang, A. C. Bovik, H. R. Sheikh, and E. P. Simoncelli, "Image quality assessment: From error visibility to structural similarity," *IEEE Trans. Medical Imaging*, vol. 13, no. 4, pp. 600–612, 2004.
- [105] I. Steinwart, D. Hush, and C. Scovel, "An explicit description of the reproducing kernel Hilbert spaces of Gaussian RBF kernels," *IEEE Transactions on Information Theory*, vol. 52, no. 10, pp. 4635–4643, 2006.
- [106] P. Bouboulis and S. Theodoridis, "Extension of Wirtinger's calculus to reproducing kernel Hilbert spaces and the complex kernel LMS," *IEEE Trans. Signal Processing*, vol. 59, no. 3, pp. 964–978, 2010.
- [107] K. Slavakis, P. Bouboulis, and S. Theodoridis, *Chapter 17: Online Learning in Reproducing Kernel Hilbert Spaces*, vol. 1 of *Academic*

Press Library in Signal Processing: Volume 1, pp. 883–987. Elsevier, Jan. 2014.

- [108] H. H. Bauschke and P. L. Combettes, *Convex Analysis and Monotone Operator Theory in Hilbert Spaces*. New York: Springer, 2011.

Supplementary File

APPENDIX A REPRODUCING KERNEL HILBERT SPACES

A feature mapping $\varphi : \mathbb{C}^\nu \rightarrow \mathcal{H}$ maps a vector $\mathbf{l} \in \mathbb{C}^\nu$ to $\varphi(\mathbf{l})$ in a feature space \mathcal{H} . To provide structured solutions, it is assumed that \mathcal{H} is a complex-valued reproducing kernel Hilbert space (RKHS), associated with a reproducing kernel $\kappa(\cdot, \cdot) : \mathbb{C}^\nu \times \mathbb{C}^\nu \rightarrow \mathbb{C}$, with rich attributes in approximation theory [35], [36], [105]–[107]. In the RKHS setting, the feature mapping becomes $\varphi(\mathbf{l}) := \kappa(\mathbf{l}, \cdot) \in \mathcal{H}$, $\forall \mathbf{l} \in \mathbb{C}^\nu$. Most well-known kernels for RKHSs are: **(i)** The linear kernel $\kappa_L(\mathbf{l}, \mathbf{l}') := \mathbf{l}^H \mathbf{l}'$, where H denotes complex conjugate vector/matrix transposition; **(ii)** the Gaussian kernel $\kappa_G; \gamma(\mathbf{l}, \mathbf{l}') := \exp[-\gamma(\mathbf{l} - \mathbf{l}')^\top (\mathbf{l} - \mathbf{l}')] [105], [106]$, where $\gamma \in \mathbb{R}_{>0}$, superscript \top stands for vector/matrix transposition, and the overline symbol denotes entry-wise complex conjugation of a scalar/vector/matrix; and **(iii)** the polynomial kernel $\kappa_P; (c, r)(\mathbf{l}, \mathbf{l}') := (\mathbf{l}^H \mathbf{l}' + c)^r$, where $r \in \mathbb{N}_*$, $c \in \mathbb{C}$. The list of kernels used for numerical tests is shown in Appendix Table IV.

TABLE IV: Dictionary of kernels.

Kernel index m	Kernel function	Parameters
1	Gaussian	$\sigma = 0.2$
2	Gaussian	$\sigma = 0.4$
3	Gaussian	$\sigma = 0.8$
4	Polynomial	$r = 1$
5	Polynomial	$r = 2$
6	Polynomial	$r = 3$
7	Polynomial	$r = 4$

APPENDIX B DERIVATION OF A COMPACT MULTI-L-KRIM DATA MODELING

By defining the ‘‘supermatrices’’

$$\begin{aligned} \mathcal{D}_1 &:= [\mathbf{D}_1^{(1)}, \mathbf{D}_2^{(1)}, \dots, \mathbf{D}_M^{(1)}] \in \mathbb{C}^{I_0 \times d_1 M}, \\ \mathcal{D}_q &:= \text{bdiag}(\mathbf{D}_1^{(q)}, \mathbf{D}_2^{(q)}, \dots, \mathbf{D}_M^{(q)}) \in \mathbb{C}^{d_{q-1} M \times d_q M}, \\ &\quad \forall q \in \{2, \dots, Q\}, \\ \mathcal{K} &:= \text{bdiag}(\mathbf{K}_1, \mathbf{K}_2, \dots, \mathbf{K}_M) \in \mathbb{C}^{MN_I \times MN_I}, \quad (17) \\ \mathcal{B} &:= [\mathbf{B}_1^H, \mathbf{B}_2^H, \dots, \mathbf{B}_M^H]^H \in \mathbb{C}^{MN_I \times I_N}, \end{aligned}$$

data modeling (8) of MultiL-KRIM, incorporated in the generic inverse problem (11), takes the form in Appendix Equation 16.

APPENDIX C SOLVING THE TVGS INVERSE PROBLEM

This section details the solutions to the TVGS sub-tasks (14a) and (14b). Sub-task (14c) involves a composite convex loss function with affine constraints which can be efficiently solved by [79].

A. Solving (14a)

Given the index set Ω , define the affine constraint $\mathcal{A}_\Omega := \{\mathbf{X} \in \mathbb{C}^{I_0 \times I_N} \mid \mathcal{S}_\Omega(\mathbf{Y}) = \mathcal{S}_\Omega(\mathbf{X})\}$, and notice that (14a) takes the form:

$$\hat{\mathbf{X}}^{(n+1/2)} = \arg \min_{\mathbf{X} \in \mathcal{A}_\Omega} \mathcal{L}_X(\mathbf{X}), \quad (18)$$

where the differentiable strongly convex loss

$$\begin{aligned} \mathcal{L}_X(\mathbf{X}) &:= \frac{1}{2} \|\mathbf{X} - \hat{\mathbf{M}}^{(n)}\|_F^2 + \frac{\lambda_L}{2} \text{tr}(\mathbf{X}^\top \mathbf{L}_\epsilon^\beta \mathbf{X} \Delta \Delta^\top) \\ &\quad + \frac{\tau_X}{2} \|\mathbf{X} - \hat{\mathbf{X}}^{(n)}\|_F^2, \end{aligned}$$

and $\hat{\mathbf{M}}^{(n)} := \hat{\mathcal{D}}_1^{(n)} \dots \hat{\mathcal{D}}_Q^{(n)} \mathcal{K} \hat{\mathcal{B}}^{(n)}$. For convenience in notations, let $\mathbf{X}_* := \hat{\mathbf{X}}^{(n+1/2)}$.

Problem (18) is a convex minimization task with affine constraints, so it can be solved iteratively by the efficient [79]. Nevertheless, (18) possesses also a closed-form solution. To formulate that closed-form solution, define the sampling matrix $\mathbf{S}_\Omega \in \mathbb{C}^{I_0 \times I_N}$ as follows: $[\mathbf{S}_\Omega]_{ij} := 1$, if $(i, j) \in \Omega$, while $[\mathbf{S}_\Omega]_{ij} := 0$, if $(i, j) \notin \Omega$. Then, $\mathcal{S}_\Omega(\mathbf{X}) = \mathbf{S}_\Omega \odot \mathbf{X}$, where \odot stands for the Hadamard product. Furthermore, define the complement set $\Omega^c := \{(i, j) \in \{1, \dots, I_0\} \times \{1, \dots, I_N\} \mid (i, j) \notin \Omega\}$. It can be verified that any $\mathbf{X} \in \mathbb{C}^{I_0 \times I_N}$ can be written as $\mathbf{X} = \mathcal{S}_\Omega(\mathbf{X}) + \mathcal{S}_{\Omega^c}(\mathbf{X}) = \mathbf{S}_\Omega \odot \mathbf{X} + \mathbf{S}_{\Omega^c} \odot \mathbf{X}$. Moreover, let $\text{vec} : \mathbb{C}^{I_0 \times I_N} \rightarrow \mathbb{C}^{I_0 I_N}$ denote the standard vectorization operator which turns matrices into vectors, and let its inverse mapping be denoted by $\text{vec}^{-1} : \mathbb{C}^{I_0 I_N} \rightarrow \mathbb{C}^{I_0 \times I_N}$. Let also the ‘‘vectorization’’ of Ω as the one-dimensional index set $\text{vec } \Omega := \{i \in \{1, \dots, I_0 I_N\} \mid [\text{vec}(\mathbf{S}_\Omega)]_i = 1\}$. Also, for any $I_0 I_N \times 1$ vector \mathbf{v} , let $\mathbf{v}|_{\text{vec } \Omega}$ be the $|\text{vec } \Omega| \times 1$ sub-vector of \mathbf{v} formed by the entries of \mathbf{v} at indices $\text{vec } \Omega$.

According to [108, Prop. 26.13], the desired solution satisfies $\mathbf{X}_* \in \mathcal{A}_\Omega \Leftrightarrow \mathcal{S}_\Omega(\mathbf{Y}) = \mathcal{S}_\Omega(\mathbf{X}_*)$ and $\nabla \mathcal{L}_X(\mathbf{X}_*) \in (\mathcal{A}_\Omega - \mathcal{S}_\Omega(\mathbf{Y}))^\perp = \{\mathbf{X} \in \mathbb{C}^{I_0 \times I_N} \mid \mathbf{0} = \mathcal{S}_\Omega(\mathbf{X})\}^\perp = \{\mathbf{X} \in \mathbb{C}^{I_0 \times I_N} \mid \mathbf{0} = \mathcal{S}_{\Omega^c}(\mathbf{X})\}$, where \perp stands for the orthogonal complement of a linear subspace. Hence,

$$\begin{aligned} \nabla \mathcal{L}_X(\mathbf{X}_*) &= (1 + \tau_X) \mathbf{X}_* + \lambda_L \mathbf{L}_\epsilon^\beta \mathbf{X}_* \Delta \Delta^\top - \hat{\mathbf{M}}^{(n)} - \tau_X \hat{\mathbf{X}}^{(n)} \\ &= (1 + \tau_X) \mathbf{X}_* + \lambda_L \mathbf{L}_\epsilon^\beta [\mathcal{S}_{\Omega^c}(\mathbf{X}_*) + \mathcal{S}_\Omega(\mathbf{X}_*)] \Delta \Delta^\top \\ &\quad - \hat{\mathbf{M}}^{(n)} - \tau_X \hat{\mathbf{X}}^{(n)} \\ &= (1 + \tau_X) \mathbf{X}_* + \lambda_L \mathbf{L}_\epsilon^\beta \mathcal{S}_{\Omega^c}(\mathbf{X}_*) \Delta \Delta^\top \\ &\quad + \lambda_L \mathbf{L}_\epsilon^\beta \mathcal{S}_\Omega(\mathbf{Y}) \Delta \Delta^\top - \hat{\mathbf{M}}^{(n)} - \tau_X \hat{\mathbf{X}}^{(n)}. \end{aligned}$$

The requirement $\mathcal{S}_{\Omega^c}(\nabla \mathcal{L}_X(\mathbf{X}_*)) = \mathbf{0}$ yields

$$\begin{aligned} (1 + \tau_X) \mathbf{S}_{\Omega^c} \odot \mathcal{S}_{\Omega^c}(\mathbf{X}_*) + \lambda_L \mathbf{S}_{\Omega^c} \odot \mathbf{L}_\epsilon^\beta \mathcal{S}_{\Omega^c}(\mathbf{X}_*) \Delta \Delta^\top \\ = -\lambda_L \mathbf{S}_{\Omega^c} \odot \mathbf{L}_\epsilon^\beta \mathcal{S}_\Omega(\mathbf{Y}) \Delta \Delta^\top + \mathbf{S}_{\Omega^c} \odot (\hat{\mathbf{M}}^{(n)} + \tau_X \hat{\mathbf{X}}^{(n)}), \end{aligned}$$

and after vectorizing by $\text{vec}(\cdot)$,

$$\begin{aligned} (1 + \tau_X) \text{diag}(\text{vec } \mathbf{S}_{\Omega^c}) \cdot \text{vec}(\mathcal{S}_{\Omega^c}(\mathbf{X}_*)) \\ + \lambda_L \text{diag}(\text{vec } \mathbf{S}_{\Omega^c}) \cdot (\Delta \Delta^\top \otimes \mathbf{L}_\epsilon^\beta) \text{vec}(\mathcal{S}_{\Omega^c}(\mathbf{X}_*)) \\ = -\lambda_L \text{diag}(\text{vec } \mathbf{S}_{\Omega^c}) \text{vec}(\mathbf{L}_\epsilon^\beta \mathcal{S}_\Omega(\mathbf{Y}) \Delta \Delta^\top) \\ + \text{diag}(\text{vec } \mathbf{S}_{\Omega^c}) \text{vec}(\hat{\mathbf{M}}^{(n)} + \tau_X \hat{\mathbf{X}}^{(n)}), \end{aligned}$$

where \otimes denotes the Kronecker product. Consequently, by keeping only the entries at indices $\text{vec}(\Omega^c)$,

$$(1 + \tau_X) \text{vec}(\mathcal{S}_{\Omega^c}(\mathbf{X}_*))|_{\text{vec}(\Omega^c)}$$

$$\mathbf{X} \approx \underbrace{\begin{bmatrix} \mathbf{D}_1^{(1)} & \mathbf{D}_2^{(1)} & \dots & \mathbf{D}_M^{(1)} \end{bmatrix}}_{\mathcal{D}_1} \underbrace{\begin{bmatrix} \mathbf{D}_1^{(2)} & 0 & \dots & 0 \\ 0 & \mathbf{D}_2^{(2)} & \dots & 0 \\ \vdots & \vdots & \ddots & \vdots \\ 0 & 0 & \dots & \mathbf{D}_M^{(2)} \end{bmatrix}}_{\mathcal{D}_2} \dots \underbrace{\begin{bmatrix} \mathbf{D}_1^{(Q)} & 0 & \dots & 0 \\ 0 & \mathbf{D}_2^{(Q)} & \dots & 0 \\ \vdots & \vdots & \ddots & \vdots \\ 0 & 0 & \dots & \mathbf{D}_M^{(Q)} \end{bmatrix}}_{\mathcal{D}_Q} \underbrace{\begin{bmatrix} \mathbf{K}_1 & 0 & \dots & 0 \\ 0 & \mathbf{K}_2 & \dots & 0 \\ \vdots & \vdots & \ddots & \vdots \\ 0 & 0 & \dots & \mathbf{K}_M \end{bmatrix}}_{\mathcal{K}} \underbrace{\begin{bmatrix} \mathbf{B}_1 \\ \mathbf{B}_2 \\ \vdots \\ \mathbf{B}_M \end{bmatrix}}_{\mathcal{B}}. \quad (16)$$

$$\begin{aligned} & + \lambda_L (\mathbf{\Delta} \mathbf{\Delta}^\top \otimes \mathbf{L}_\epsilon^\beta) |_{\text{vec}(\Omega^b) \times \text{vec}(\Omega^b)} \cdot \text{vec}(\mathcal{S}_{\Omega^b}(\mathbf{X}_*)) |_{\text{vec}(\Omega^b)} \\ & = -\lambda_L \text{vec}(\mathbf{L}_\epsilon^\beta \mathcal{S}_\Omega(\mathbf{Y}) \mathbf{\Delta} \mathbf{\Delta}^\top) |_{\text{vec}(\Omega^b)} \\ & \quad + \text{vec}(\hat{\mathbf{M}}^{(n)} + \tau_X \hat{\mathbf{X}}^{(n)}) |_{\text{vec}(\Omega^b)}, \end{aligned}$$

where $(\mathbf{\Delta} \mathbf{\Delta}^\top \otimes \mathbf{L}_\epsilon^\beta) |_{\text{vec}(\Omega^b) \times \text{vec}(\Omega^b)}$ is the submatrix extracted from $\mathbf{\Delta} \mathbf{\Delta}^\top \otimes \mathbf{L}_\epsilon^\beta$ by keeping only the rows and columns indicated by $\text{vec}(\Omega^b)$. It can be readily verified that

$$\begin{aligned} & \text{vec}(\mathcal{S}_{\Omega^b}(\mathbf{X}_*)) |_{\text{vec}(\Omega^b)} \\ & = \left((1 + \tau_X) \mathbf{I}_{|\text{vec}(\Omega^b)|} + \lambda_L (\mathbf{\Delta} \mathbf{\Delta}^\top \otimes \mathbf{L}_\epsilon^\beta) |_{\text{vec}(\Omega^b) \times \text{vec}(\Omega^b)} \right)^{-1} \\ & \quad \cdot \left(-\lambda_L \text{vec}(\mathbf{L}_\epsilon^\beta \mathcal{S}_\Omega(\mathbf{Y}) \mathbf{\Delta} \mathbf{\Delta}^\top) |_{\text{vec}(\Omega^b)} \right. \\ & \quad \left. + \text{vec}(\hat{\mathbf{M}}^{(n)} + \tau_X \hat{\mathbf{X}}^{(n)}) |_{\text{vec}(\Omega^b)} \right). \quad (19) \end{aligned}$$

Recovering $\mathcal{S}_{\Omega^b}(\mathbf{X}_*)$ from (19) is a straightforward task: take an all-zero $I_0 I_N \times 1$ vector, replace its zero entries at positions $\text{vec}(\Omega^b)$ by the corresponding entries of (19), and then apply $\text{vec}^{-1}(\cdot)$ to recover $\mathcal{S}_{\Omega^b}(\mathbf{X}_*)$. Finally,

$$\begin{aligned} \hat{\mathbf{X}}^{(n+1/2)} & = \mathbf{X}_* = \mathcal{S}_\Omega(\mathbf{X}_*) + \mathcal{S}_{\Omega^b}(\mathbf{X}_*) \\ & = \mathcal{S}_\Omega(\mathbf{Y}) + \mathcal{S}_{\Omega^b}(\mathbf{X}_*). \end{aligned}$$

B. Solving (14b)

For compact notations, let $\hat{\mathcal{D}}_{Q+1}^{(n)} := \mathcal{K}$ and $\hat{\mathcal{D}}_{Q+2}^{(n)} := \hat{\mathcal{B}}^{(n)}$. For any $q \in \{2, \dots, Q\}$, define

$$\begin{aligned} \hat{\mathbf{L}}_q^{(n)} & := \prod_{q'=1}^{q-1} \hat{\mathcal{D}}_{q'}^{(n)}, \\ \hat{\mathbf{R}}_q^{(n)} & := \prod_{q'=q+1}^{Q+2} \hat{\mathcal{D}}_{q'}^{(n)}, \end{aligned}$$

while $\hat{\mathbf{L}}_1^{(n)} := \mathbf{I}_{I_0}$ and $\hat{\mathbf{R}}_1^{(n)} := \prod_{q'=2}^{Q+2} \hat{\mathcal{D}}_{q'}^{(n)}$, so that the gradient of the loss in (14b) takes the form

$$\begin{aligned} \nabla \mathcal{L}_D(\mathcal{D}_q) & = \hat{\mathbf{L}}_q^{(n)} \mathcal{D}_q \hat{\mathbf{R}}_q^{(n)} - \hat{\mathbf{X}}^{(n)} \\ & \quad + \lambda_2 \mathcal{D}_q + \tau_D (\mathcal{D}_q - \hat{\mathcal{D}}_q^{(n)}). \end{aligned}$$

The solution $\hat{\mathcal{D}}_q^{(n+1/2)}$ to (14b) takes a closed form, and the way to obtain it follows the steps of Appendix C-A, where the affine constraint to amount for the block-diagonal form of \mathcal{D}_q , for $q \in \{2, \dots, Q\}$, becomes $\mathcal{A}_\Omega := \{\mathcal{D}_q \in \mathbb{C}^{d_{q-1}M \times d_qM} \mid \mathbf{0} = \mathcal{S}_\Omega(\mathcal{D}_q)\}$, with the index set Ω comprising all pairs of indices positioned off the diagonal blocks. In the case of \mathcal{D}_1 , no affine constraint (no block-diagonal structure) is necessary to solve (14b). Solving $\nabla \mathcal{L}_D(\mathcal{D}_1) = \mathbf{0}$ for \mathcal{D}_1 will do the job.

APPENDIX D

SOLVING THE DMRI INVERSE PROBLEM

This section expands the details of the dMRI inverse problem (15). Similarly to the discussion in Section IV-B, and upon defining the following tuple of estimates $\forall n \in \mathbb{N}, \forall k \in \{0, 1\}$,

$$\begin{aligned} \hat{\mathcal{O}}^{(n+k/2)} & := (\hat{\mathbf{X}}^{(n+k/2)}, \hat{\mathbf{Z}}^{(n+k/2)}, \hat{\mathcal{D}}_1^{(n+k/2)}, \\ & \quad \dots, \hat{\mathcal{D}}_Q^{(n+k/2)}, \hat{\mathcal{B}}^{(n+k/2)}), \quad (20) \end{aligned}$$

Algorithm 1 solves (15) via computing solutions of the following convex sub-tasks:

$$\begin{aligned} \hat{\mathbf{X}}^{(n+1/2)} & \in \arg \min_{\mathbf{X}} \frac{1}{2} \|\mathbf{X} - \hat{\mathcal{D}}_1^{(n)} \dots \hat{\mathcal{D}}_Q^{(n)} \mathcal{K} \hat{\mathcal{B}}^{(n)}\|_{\text{F}}^2 \\ & \quad + \frac{\lambda_2}{2} \|\hat{\mathbf{Z}}^{(n)} - \mathcal{F}_t(\mathbf{X})\|_{\text{F}}^2 \\ & \quad + \frac{\tau_X}{2} \|\mathbf{X} - \hat{\mathbf{X}}^{(n)}\|_{\text{F}}^2 \\ & \quad \text{s.t. } \mathcal{S}_\Omega(\mathbf{Y}) = \mathcal{S}_\Omega \mathcal{F}(\mathbf{X}), \quad (21a) \end{aligned}$$

$$\begin{aligned} \hat{\mathbf{Z}}^{(n+1/2)} & \in \arg \min_{\mathbf{Z}} \frac{\lambda_2}{2} \|\mathbf{Z} - \mathcal{F}_t(\hat{\mathbf{X}}^{(n)})\|_{\text{F}}^2 + \lambda_3 \|\mathbf{Z}\| \\ & \quad + \frac{\tau_Z}{2} \|\mathbf{Z} - \hat{\mathbf{Z}}^{(n)}\|_{\text{F}}^2, \quad (21b) \end{aligned}$$

$$\begin{aligned} \hat{\mathcal{D}}_q^{(n+1/2)} & \in \arg \min_{\mathcal{D}_q} \frac{1}{2} \|\hat{\mathbf{X}}^{(n)} - \hat{\mathcal{D}}_1^{(n)} \dots \mathcal{D}_q \dots \hat{\mathcal{D}}_Q^{(n)} \mathcal{K} \hat{\mathcal{B}}^{(n)}\|_{\text{F}}^2 \\ & \quad + \frac{\lambda_4}{2} \|\mathcal{D}_q\|_{\text{F}}^2 + \frac{\tau_D}{2} \|\mathcal{D}_q - \hat{\mathcal{D}}_q^{(n)}\|_{\text{F}}^2, \\ & \quad \text{s.t. } \mathcal{D}_q \text{ is block diagonal } \forall q \in \{2, \dots, Q\}, \quad (21c) \end{aligned}$$

$$\begin{aligned} \hat{\mathcal{B}}^{(n+1/2)} & \in \arg \min_{\mathcal{B}} \frac{1}{2} \|\hat{\mathbf{X}}^{(n)} - \hat{\mathcal{D}}_1^{(n)} \dots \hat{\mathcal{D}}_Q^{(n)} \mathcal{K} \mathcal{B}\|_{\text{F}}^2 \\ & \quad + \lambda_1 \|\mathcal{B}\|_1 + \frac{\tau_B}{2} \|\mathcal{B} - \hat{\mathcal{B}}^{(n)}\|_{\text{F}}^2 \\ & \quad \text{s.t. } \mathbf{1}_{N_t}^H \mathcal{B}_m = \mathbf{1}_{I_N}^H, \forall m \in \{1, \dots, M\}. \quad (21d) \end{aligned}$$

Sub-task (21d) is composite convex with affine constraints and can be solved by [79]; details are provided in [48]. Sub-task (21c) is similar to sub-task (14b) of the TVGS case, so that its solution follows Appendix C-B. The following are the solutions to sub-tasks (21a) and (21b).

A. Solving (21a)

Following [48], the unique solution $\hat{\mathbf{X}}^{(n+1/2)}$ to (14a) is

$$\begin{aligned} \hat{\mathbf{X}}^{(n+1/4)} & := C_X \left(\hat{\mathbf{M}}^{(n)} + \lambda_2 I_N \mathcal{F}_t^{-1}(\hat{\mathbf{Z}}^{(n)}) + \tau_X \hat{\mathbf{X}}^{(n)} \right), \\ \hat{\mathbf{X}}^{(n+1/2)} & := \mathcal{F}^{-1} \mathcal{S}_\Omega(\mathbf{Y}) + \mathcal{F}^{-1} \mathcal{S}_{\Omega^b} \mathcal{F}(\hat{\mathbf{X}}^{(n+1/4)}), \end{aligned}$$

where $C_X := 1/(1 + \lambda_2 I_N + \tau_X)$.

B. Solving (21b)

Consider a convex function $g(\cdot) : \mathbb{C}^{m \times n} \rightarrow \mathbb{R} \cup \{+\infty\}$ and $\lambda \in \mathbb{R}_{>0}$. The proximal mapping $\text{Prox}_{\lambda g}(\cdot) : \mathbb{C}^{m \times n} \rightarrow$

$\mathbb{C}^{m \times n}$ is defined as $\text{Prox}_{\lambda g}(\mathbf{A}) := \arg \min_{\mathbf{B} \in \mathbb{C}^{m \times n}} \lambda g(\mathbf{B}) + (1/2) \|\mathbf{A} - \mathbf{B}\|_F^2$ [108]. When g is the ℓ_1 -norm $\|\cdot\|_1$, the (i, j) th entry of $\text{Prox}_{\lambda \|\cdot\|_1}(\mathbf{A})$ is obtained by the soft-thresholding rule [108]:

$$[\text{Prox}_{\lambda \|\cdot\|_1}(\mathbf{A})]_{ij} = [\mathbf{A}]_{ij} \left(1 - \frac{\lambda}{\max\{\lambda, |[A]_{ij}|\}}\right). \quad (22)$$

Instead of $\text{Prox}_{\lambda \|\cdot\|_1}(\mathbf{A})$, it is more common to use notation $\text{Soft}(\mathbf{A}, \lambda)$. As such, the solution $\hat{\mathbf{Z}}^{(n+1/2)}$ of (21b) is provided by

$$\hat{\mathbf{Z}}^{(n+1/2)} = \text{Soft}[\mathcal{F}_t(\hat{\mathbf{X}}^{(n)}) + \frac{\tau_Z}{\lambda_2} \hat{\mathbf{Z}}^{(n)}, \frac{\lambda_3}{\lambda_2}].$$

APPENDIX E

MORE RESULTS FOR TVGS RECOVERY

This section provides additional figures and tables containing experimental results of TVGS recovery (cf., Section IV-C).

TABLE V: Categorization of TVGS recovery methods.

Method	Factorization/structured	Low-rank	Kernel-based
GraphTRSS [77]	✗	✗	✗
KRG [55]	✓	✗	✓
KGL [54]	✓	✗	✓
LRDS [70]	✗	✓	✗
MMF [14]	✓	✓	✗
NBP [30]	✓	✓	✓
MultiL-KRIM	✓	✓	✓

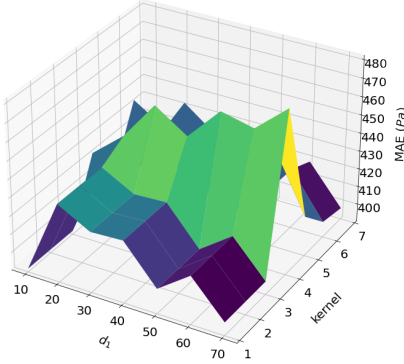


Fig. 6: Sensitivity of MAE to variation of parameters d_1 and kernel choice in the context of (D3, P1, Nav1, L1) at 10% sampling ratio.

A. Performance metrics

Recall that the original TVGS data is \mathbf{Y} and the reconstructed data is \mathbf{X} , which are both matrices of size $I_0 \times I_N$. The error metrics are defined as follows,

$$\begin{aligned} \text{RMSE} &:= \frac{\|\mathbf{X} - \mathbf{Y}\|_F}{\sqrt{I_0 \cdot I_N}}, \\ \text{MAE} &:= \frac{\|\mathbf{X} - \mathbf{Y}\|_1}{I_0 \cdot I_N}, \\ \text{MAPE} &:= \frac{1}{I_0 \cdot I_N} \sum_{i=1}^{I_0} \sum_{j=1}^{I_N} \left| \frac{x_{ij} - y_{ij}}{y_{ij}} \right|. \end{aligned}$$

B. Navigator- and landmark-point analysis

To examine the effect of different navigator-data formation and landmark-point selection strategies, tests are conducted on the (D1, P1, ·, ·) scenario. Appendix Table VI shows the

error metrics of MultiL-KRIM under scenario (D1, P1, ·, L1) when using different navigator-data formations. Averaged over all sampling ratios, navigator data created from snapshots (Nav1) have advantage over other formations, while those formed by nodes signals (Nav2) produce highest errors. On the other hand, Appendix Table VII depicts variants of landmark-point selection strategies under scenario (D1, P1, Nav1, ·). Overall, there is no significant difference when using maxmin or clustering methods for landmark-point selection.

TABLE VI: Performance on different navigators formation strategies under scenario (D1, P1, ·, L1).

Sampling ratio	Metric	Nav1	Nav2	Nav3	Nav4
0.1	MAE	0.3004	0.3562	0.3350	0.3130
	RMSE	0.4211	0.5065	0.5055	0.4219
	MAPE	0.0296	0.0299	0.0283	0.0271
0.2	MAE	0.1732	0.1794	0.1883	0.1811
	RMSE	0.2741	0.2899	0.3046	0.2872
	MAPE	0.0175	0.0195	0.0200	0.0194
0.3	MAE	0.1176	0.1313	0.1213	0.1303
	RMSE	0.1861	0.2074	0.1916	0.2045
	MAPE	0.0137	0.0157	0.0150	0.0158
0.4	MAE	0.0824	0.0865	0.0834	0.0812
	RMSE	0.1607	0.1699	0.1643	0.1635
	MAPE	0.0082	0.0089	0.0082	0.0084
0.5	MAE	0.0562	0.0638	0.0585	0.0608
	RMSE	0.1155	0.0994	0.0998	0.0949
	MAPE	0.0050	0.0059	0.0050	0.0058
Average	MAE	0.1460	0.1635	0.1573	0.1533
	RMSE	0.2315	0.2546	0.2532	0.2344
	MAPE	0.0148	0.0160	0.0153	0.0153

TABLE VII: Performance on different landmark points selection strategies under scenario (D1, P1, Nav1, ·).

Sampling ratio	Metric	L1	L2	L3
0.1	MAE	0.3004	0.3134	0.3290
	RMSE	0.4211	0.4180	0.4587
	MAPE	0.0296	0.0285	0.0291
0.2	MAE	0.1732	0.1785	0.1796
	RMSE	0.2741	0.2847	0.2954
	MAPE	0.0175	0.0179	0.0190
0.3	MAE	0.1176	0.1193	0.1166
	RMSE	0.1861	0.1885	0.1848
	MAPE	0.0137	0.0144	0.0144
0.4	MAE	0.0824	0.0819	0.0811
	RMSE	0.1607	0.1605	0.1596
	MAPE	0.0082	0.0083	0.0082
0.5	MAE	0.0562	0.0565	0.0551
	RMSE	0.1155	0.0998	0.0996
	MAPE	0.0050	0.0048	0.0048
Average	MAE	0.1460	0.1499	0.1523
	RMSE	0.2315	0.2303	0.2396
	MAPE	0.0148	0.0147	0.0151

TABLE VIII: Runtime comparison (in seconds) between LRDS and MultiL-KRIM in dataset D3.

Sampling pattern	Sampling rate	LRDS	MultiL-KRIM	Speedup
P1	0.1	1,393	413	3.4x
	0.2	1,468	490	3x
	0.3	1,358	719	1.9x
	0.4	1,356	330	4.1x
	0.5	1,346	270	5x
P2	0.1	1,433	545	2.6x
	0.2	1,430	465	3.1x
	0.3	1,463	461	3.2x
	0.4	1,487	428	3.5x
	0.5	1,470	562	2.6x

TABLE IX: Number of parameter unknowns (9)

Q	$\{d_q\}_{q=1}^{Q-1}$	$N_Q[M=1]$	$N_Q[M=7]$
1	–	11,677,680	81,743,760
2	{8}	1,357,472	9,502,304
3	{2, 8}	358,704	2,510,928

TABLE X: Number of parameter unknowns of MultiL-KRIM and TDDIP

Method	Number of parameter unknowns
MultiL-KRIM[$M=7, Q=2$]	9,502,304
MultiL-KRIM[$M=1, Q=2$]	1,357,472
MultiL-KRIM[$M=7, Q=3$]	2,510,928
MultiL-KRIM[$M=1, Q=3$]	358,704
TDDIP ¹	3,162,025
TDDIP ²	2,492,713
TDDIP ³	394,985
TDDIP ⁴	255,417

TABLE XI: Performance of MultiL-KRIM and TDDIP on radial sampling (acceleration rate: 16x)

Methods \ Metrics	NRMSE	SSIM	HFEN	M1	M2	Time
MultiL-KRIM[$M=7, Q=2$]	0.0448	0.8680	0.1023	37.35	1.4×10^6	1.2hrs
MultiL-KRIM[$M=1, Q=2$]	0.0465	0.8618	0.1305	37.26	1.4×10^6	44min
MultiL-KRIM[$M=7, Q=3$]	0.0448	0.8675	0.1030	37.35	1.4×10^6	1hr
MultiL-KRIM[$M=1, Q=3$]	0.0465	0.8618	0.1305	37.26	1.4×10^6	41min
TDDIP ¹ [27]	0.0376	0.8896	0.1452	36.24	1.3×10^6	3.9hrs
TDDIP ² [27]	0.0388	0.8855	0.1464	35.14	1.3×10^6	3.5hrs
TDDIP ³ [27]	0.0415	0.8691	0.1642	35.87	1.4×10^6	2hrs
TDDIP ⁴ [27]	0.0422	0.8680	0.1668	35.68	1.4×10^6	1.2hrs

APPENDIX F

MORE RESULTS ON DMRI RECONSTRUCTION

For demonstration, Appendix Table X examines different sizes of TDDIP by varying the number of layers and hidden dimensions, where TDDIP¹ is the setting scoring the lowest NRMSE, TDDIP² and TDDIP³ are close to MultiL-KRIM[$M=7, Q=3$] and MultiL-KRIM[$M=1, Q=3$] in number of parameters, respectively, while TDDIP⁴ matches the computational times of [$M=7$]. Specifically, performance of these variations of TDDIP are reported in Appendix Table XI. Note that if the complexity of TDDIP decreases, its NRMSE and SSIM approach those of MultiL-KRIM. Nevertheless, increasing the number of unknowns of MultiL-KRIM, whether by increasing the number of kernels M or adopting larger inner dimensions, does not significantly improve its performance. These findings suggest a research direction of developing a “deep” architecture for MultiL-KRIM, e.g., by adding non-linear activation function layers into its factorization, inspired by results showing that deep matrix factorization outperforms the standard MMF in matrix completion tasks [15], [16]. More results on this research front will be reported at other publication venues.

Dataset	Sampling ratio	Metric	LRDS	GraphTRSS	KRG	KGL	MMF	NBP	MultiL-KRIM
Sea Temperature	0.1	MAE	0.3450	0.5822	0.4487	0.4438	0.3338	0.3009	0.3004
		RMSE	0.5615	0.8645	0.5906	0.5824	0.4773	0.4018	0.4211
		MAPE	0.0327	0.0507	0.0430	0.0405	0.0277	0.0269	0.0296
	0.2	MAE	0.1817	0.3200	0.2478	0.2352	0.1758	0.1726	0.1732
		RMSE	0.2814	0.5168	0.4156	0.4049	0.2806	0.2756	0.2741
		MAPE	0.0186	0.0295	0.0222	0.0211	0.0185	0.0182	0.0175
	0.3	MAE	0.1185	0.2093	0.1669	0.1649	0.1199	0.1206	0.1176
		RMSE	0.1867	0.3659	0.2880	0.2832	0.1901	0.1903	0.1861
		MAPE	0.0131	0.0200	0.0171	0.0169	0.0140	0.0142	0.0137
	0.4	MAE	0.0857	0.1400	0.1103	0.1153	0.0847	0.0840	0.0824
		RMSE	0.1422	0.2584	0.2328	0.2438	0.1662	0.1643	0.1607
		MAPE	0.0098	0.0145	0.0092	0.0093	0.0083	0.0079	0.0082
	0.5	MAE	0.0621	0.0982	0.0749	0.0782	0.0602	0.0566	0.0562
		RMSE	0.1079	0.1966	0.1236	0.1292	0.0941	0.0889	0.1155
		MAPE	0.0066	0.0101	0.0061	0.0063	0.0052	0.0055	0.0050
PM2.5 Concentration	0.1	MAE	2.586	2.7698	2.5111	2.5214	2.3684	2.2936	2.2759
		RMSE	4.558	4.7418	4.8145	4.8593	4.3193	4.2110	4.1863
		MAPE	0.4928	0.4558	0.4778	0.4815	0.3941	0.3758	0.4053
	0.2	MAE	2.0248	2.1572	1.7916	1.8028	1.7688	1.7041	1.6893
		RMSE	3.7212	3.6645	3.3176	3.3203	3.2665	3.2666	3.1932
		MAPE	0.3413	0.3765	0.3003	0.2994	0.3028	0.2890	0.2898
	0.3	MAE	1.6123	1.7004	1.5179	1.4923	1.4380	1.3917	1.3255
		RMSE	3.10697	3.0457	3.1716	3.1646	3.0090	2.9376	2.6244
		MAPE	0.2907	0.292	0.2440	0.2380	0.2336	0.2347	0.2354
	0.4	MAE	1.2519	1.4574	1.1746	1.1553	1.1251	1.0994	1.0342
		RMSE	2.5083	2.6089	2.5277	2.5188	2.4154	2.3277	2.2939
		MAPE	0.2504	0.2554	0.1947	0.1912	0.1933	0.1911	0.1668
Sea Level Pressure	0.1	MAE	432.3553	438.5799	436.2410	435.4914	409.7814	408.8739	393.5182
		RMSE	653.6381	673.0891	675.2066	678.8780	619.8458	618.0385	577.7076
		MAPE	0.0044	0.0043	0.0041	0.0041	0.0040	0.0040	0.0038
	0.2	MAE	315.3191	340.9664	323.9920	321.1525	293.8725	290.9654	277.9168
		RMSE	502.2517	558.7858	555.1179	523.1133	477.8935	481.9912	463.2686
		MAPE	0.0031	0.0034	0.0032	0.0029	0.0028	0.0028	0.0027
	0.3	MAE	254.9302	275.5929	264.8433	261.0184	220.3090	220.6122	208.6543
		RMSE	418.5478	476.5155	443.2093	430.8483	377.7021	380.5985	363.3772
		MAPE	0.0025	0.0027	0.0025	0.0023	0.0023	0.0023	0.0021
	0.4	MAE	201.3499	224.1063	206.5154	206.9803	162.9623	163.7134	158.0415
		RMSE	352.2565	412.6796	367.3505	355.3074	303.4321	311.2039	296.1789
		MAPE	0.0021	0.0022	0.0019	0.0018	0.0016	0.0016	0.0016
	0.5	MAE	154.1453	179.4160	169.0522	163.3182	130.1137	123.4560	119.3680
		RMSE	296.6426	352.4861	319.3949	321.6328	290.1288	269.4014	278.5416
		MAPE	0.0015	0.0018	0.0016	0.0015	0.0013	0.0012	0.0012

TABLE XII: Performance comparisons for Random Sampling (P1). Red-colored numbers are lowest errors.

Dataset	Sampling ratio	Metric	LRDS	GraphTRSS	KRG	KGL	MMF	NBP	MultiL-KRIM
Sea Temperature	0.1	MAE	1.1540	1.2054	1.1705	1.1617	1.0946	1.0850	0.9966
		RMSE	1.6223	1.7232	1.6684	1.6596	1.4288	1.4154	1.3542
		MAPE	0.1172	0.1247	0.1172	0.1171	0.1175	0.1164	0.1157
	0.2	MAE	0.8621	0.9962	0.8935	0.8786	0.8161	0.7927	0.7762
		RMSE	1.3173	1.5442	1.2882	1.2840	1.2215	1.2202	1.1768
		MAPE	0.0898	0.1040	0.0930	0.0922	0.0950	0.0892	0.0865
	0.3	MAE	0.6333	0.6421	0.6223	0.6161	0.5879	0.5803	0.5609
		RMSE	1.0650	1.1240	1.0641	1.0697	1.0241	1.0148	0.9876
		MAPE	0.0670	0.0653	0.0645	0.0638	0.0575	0.0566	0.0557
	0.4	MAE	0.4536	0.4520	0.4023	0.4018	0.3905	0.3876	0.3770
		RMSE	0.8274	0.8495	0.7676	0.7645	0.7366	0.7345	0.7211
		MAPE	0.0509	0.0467	0.0419	0.0419	0.0407	0.0403	0.0385
	0.5	MAE	0.2663	0.3063	0.2831	0.2825	0.2605	0.2615	0.2560
		RMSE	0.5450	0.5934	0.5912	0.5855	0.5580	0.5525	0.5435
		MAPE	0.0263	0.0350	0.0308	0.0306	0.0306	0.0303	0.0292
PM2.5 Concentration	0.1	MAE	3.5170	3.7224	3.2365	3.2133	3.2120	3.1685	3.0717
		RMSE	5.7922	6.5506	5.4857	5.4166	5.3981	5.3666	5.2669
		MAPE	0.5125	0.5987	0.5828	0.4831	0.4811	0.5309	0.5278
	0.2	MAE	2.5809	2.7509	2.5363	2.5412	2.4906	2.4782	2.4226
		RMSE	4.4577	4.8055	4.5982	4.6150	4.6008	4.5416	4.2820
		MAPE	0.4588	0.5110	0.4598	0.4614	0.4834	0.4863	0.4717
	0.3	MAE	2.0887	2.1562	2.0231	2.0161	1.9740	1.9534	1.9405
		RMSE	4.1175	4.0359	3.9335	3.9242	3.8544	3.8286	3.8262
		MAPE	0.3420	0.3872	0.3613	0.3574	0.3583	0.3541	0.3452
	0.4	MAE	1.7716	1.7880	1.5922	1.5841	1.5715	1.5508	1.5285
		RMSE	3.6206	3.5443	3.3331	3.3171	3.3405	3.3078	3.1535
		MAPE	0.2983	0.3133	0.2796	0.2760	0.2809	0.2786	0.2737
	0.5	MAE	1.4244	1.5043	1.2903	1.2876	1.2904	1.2867	1.2645
		RMSE	2.9851	3.1396	2.9521	2.9361	2.9533	2.9315	2.8521
		MAPE	0.2506	0.2260	0.2477	0.2375	0.2303	0.2283	0.2504
Sea Level Pressure	0.1	MAE	452.3376	469.8179	460.6198	459.5086	457.6376	452.2161	444.3823
		RMSE	673.5309	704.6300	722.8781	715.2535	714.0710	707.0870	696.8868
		MAPE	0.0045	0.0046	0.0048	0.0047	0.0047	0.0045	0.0044
	0.2	MAE	395.4735	404.9930	376.2283	374.5962	365.2090	360.5889	355.2410
		RMSE	602.4211	609.5108	641.7902	606.5960	582.4397	581.1579	578.3478
		MAPE	0.0039	0.0040	0.0038	0.0038	0.0037	0.0036	0.0035
	0.3	MAE	319.3464	328.3074	309.2513	308.1569	298.5832	296.9049	293.2719
		RMSE	535.5085	547.2752	547.0275	537.0053	525.3399	521.1263	513.2530
		MAPE	0.0034	0.0034	0.0030	0.0030	0.0030	0.0030	0.0029
	0.4	MAE	265.9806	274.8237	251.6239	251.0470	249.6740	246.4856	243.6812
		RMSE	483.8443	476.1510	479.6474	480.5829	469.6758	461.5433	456.8314
		MAPE	0.0028	0.0027	0.0026	0.0026	0.0025	0.0025	0.0025
	0.5	MAE	222.3163	224.0090	206.3858	205.5674	200.1395	198.1765	195.2719
		RMSE	408.2798	413.9014	428.3704	429.2268	411.1974	370.1874	398.6022
		MAPE	0.0022	0.0022	0.0021	0.0021	0.0020	0.0020	0.0020

TABLE XIII: Performance comparisons for Entire Snapshots Sampling (P2). Red-colored numbers are lowest errors.